J. Fluid Mech. (2002), *vol.* 456, *pp.* 49–84.
DOI: 10.1017/S0022112001007418 Printed in the United Kingdom

Mechanisms and passive control of crossflow-vortex-induced transition in a three-dimensional boundary layer

By PETER WASSERMANN AND MARKUS KLOKER

Institut für Aerodynamik und Gasdynamik, Universität Stuttgart, Pfaffenwaldring 21, D-70550 Stuttgart, Germany

(Received 30 April 2001 and in revised form 11 September 2001)

Crossflow-vortex-induced laminar breakdown in a three-dimensional flat-plate boundary-layer flow is investigated in detail by means of spatial direct numerical simulations. The base flow is generic for an infinite swept wing, with decreasing favourable chordwise pressure gradient. First, the downstream growth and nonlinear saturation states initiated by a crossflow-vortex-mode packet as well as by single crossflow-vortex modes with various spanwise wavenumbers are simulated. Second, the secondary instability of the flow induced by the saturated crossflow vortices is scrutinized, clearly indicating the convective nature of the secondary instability and strengthening knowledge of the conditions for its onset. Emphasis is on the effect of crossflow-vortex-mode packets and of the spanwise vortex spacing on the secondary stability properties of the saturation states. Saturated uniform crossflow vortices initiated by single crossflow-vortex modes turn out to be less unstable than vortices initiated by a packet of vortex modes, and closely spaced saturated vortices are even stable. Third, we investigate the transition control strategy of upstream flow deformation by appropriate steady nonlinear vortex modes as applied in wind tunnel experiments at the Arizona State University. A significant transition delay is shown in the base flow considered here, and the underlying mechanisms are specified.

1. Introduction

On a swept-back wing the chordwise acceleration of the potential flow induces an inboard-oriented crossflow component inside the boundary layer perpendicular to the mean flow direction. The crossflow velocity profile $w_s(y)$, y being the wall-normal coordinate, is inflectional and causes a strong primary instability of the flow with respect to so-called crossflow modes that can be steady or unsteady. The unsteady disturbances have been found to be dominant at high free-stream-turbulence conditions, where they are generated on higher amplitude levels and suppress the development of the unstable steady modes. At low free-stream-turbulence conditions as in free flight, steady crossflow vortex modes excited even by minute surface non-uniformity or roughness are found to be dominant, although the maximal primary amplification is for unsteady disturbances. Consequently, most investigations on laminar–turbulent transition in three-dimensional boundary-layer flows focus on steady crossflow modes as the primary disturbances. Upon downstream amplitude saturation, high-amplitude crossflow vortices oriented in the streamwise direction are formed, which distort the flow field and cause strong shear layers that trigger

a subsequent 'explosive' secondary instability mechanism finally leading to laminar breakdown.

Most concentrated experimental work on the subject, employing controlled experiments with well-defined artificial disturbance input, has been done by three groups: at DLR Göttingen, Germany, by Bippes, Deyhle, Lerche and co-workers; at the unsteady wind tunnel facility of the Arizona State University (ASU) by Saric, White and others (for reviews, including work of others, see Bippes 1999 and Saric, Carrillo & Reibert 1998*b*); and at Tohoku University, Sendai, by Kawakami, Kohama & Okutsu (1999). In the DLR experiments on a flate plate emphasis has been on the nonlinear interaction between steady and unsteady primary crossflow modes and on the resulting transition scenarios. The steady vortices have been found to dominate in low-turbulence conditions, whereas the unsteady crossflow waves dominate in a high-turbulence environment. In the vortex-dominated scenarios a secondary high-frequency instability has been observed that undergoes an explosive growth and triggers transition. In the regime dominated by a single crossflow wave, slowly proceeding transition with a gradual widening of the Fourier spectrum of the unsteady disturbance motion is found (see Deyhle & Bippes 1996 and Lerche 1996). On the other hand the ASU experiments focus on the vortex-dominated transition scenario in low-turbulence conditions on a model wing. First, the nonlinear development and saturation of crossflow vortices initiated by varied controlled disturbance excitation was under investigation (see Radeztsky, Reibert & Saric 1999; Reibert, Saric & Carrillo 1996; Reibert & Saric 1997). Recently, the secondary high-frequency instability, first observed by Kohama, Saric & Hoos (1991), has been measured in detail for different initial steady conditions (see White *et al.* 2001; White & Saric 2002). Kawakami *et al.* experimentally investigated the crossflow-vortex-induced secondary instability on a flate plate under controlled disturbance excitation for both the primary steady and the secondary unsteady instabilities.

In parallel, a number of theoretical investigations on this topic has been performed. Typically, the parabolized stability equations (PSE) are used to calculate nonlinear states of the primary unstable steady crossflow vortices, see e.g. Malik, Li & Chang (1994), Malik *et al.* (1999), Haynes & Reed (1996, 2000), Janke & Balakumar (2000) and the more general review by Reed, Haynes & Saric (1998). In the detailed work of Koch *et al.* (2000) nonlinear equilibrium solutions are also used, and the saturation amplitudes of both PSE and equilibrium solutions are compared to results of direct numerical simulations of Bonfigli & Kloker (1999), showing reasonably good agreement. Subsequently, Floquet theory is employed for a temporal secondary instability theory where, unlike the theory for two-dimensional boundary layers, two-dimensional eigenfunctions spanning the crosswise cut through the flow field are necessary. The instability is, like in the experiments, localized in physical rather than in spectral frequency–spanwise wavenumber space, the latter being an inadequate and often even misleading analysis basis in the case of three-dimensional boundary layers. (We note that for secondary instability in two-dimensional boundary layers, induced by a large-amplitude two-dimensional Tollmien–Schlichting wave, the frequency–spanwise wavenumber space is the successful basis because the 'shape assumption' holds, i.e. higher modes nonlinearly generated by the grown primary TS disturbance do not play a significant role at secondary-instability onset.)

Principally, three different classes of secondary instability modes were identified (the letter notation follows the suggestion of Malik *et al.* 1999): (i) the high-frequency 'mode I' or 'z' mode, induced by the minimum of the spanwise gradient of the streamwise velocity component, (ii) the high-frequency 'mode II' or 'y' mode, induced

by the local maximum of the wall-normal gradient; and (iii) the low-frequency 'mode III', most likely linked to the maximum of the spanwise gradient. The modes exhibit their amplitude maxima in the respective regions of the deformed three-dimensional mean flow, i.e. the most amplified 'z' mode is located at the updraught crossflow vortex side, and the 'y' mode on top of the vortex. The weaker amplified mode-III class is found under the vortex close to the wall. The PSE approach has proven to yield reliable results for the primary saturated steady states at computational costs typically lower than for a direct numerical simulation. With the secondary stability theory the full local instability spectrum is obtained indicating the secondary instability properties of a given primary state. Since temporal amplification rates in a vortex-oriented coordinate system are calculated, no *a priori* answer to the relevance of the found modes and their instability nature – convective or absolute – can be given. In fact, in experiments predominantly the 'z' mode has been observed, whereas the theory often quantifies a 'y' mode to be the most unstable mode. No PSE calculations for the secondary instability have been reported so far, possibly due to the comparably large computation time and storage requirements. Regarding the nature of the instability, special investigations were first performed by Lingwood (1997). The results, indicating a 'chordwise absolute instability', caused an intensive discussion about its relevance, and gave rise to new theoretical work, see e.g. Koch (2002). However, no clear picture can be given yet.

Direct numerical simulations (DNS) of transition phenomena in three-dimensional boundary layers were performed using two models: (i) the temporal model (TDNS), with periodic directions along and perpendicular to the crossflow vortices and thus predetermined timewise disturbance growth; and (ii) the computationally more demanding spatial model (SDNS), with free disturbance growth and periodicity in the plate/body-fixed spanwise direction only. Various TDNS were performed by Kleiser and co-workers, most recently by Wintergerste & Kleiser (1996, 1997) (earlier work of the Kleiser group is referenced therein). They identified and traced flow structures during breakdown for different initial conditions and spotted a secondary vortex involved in the transition process, which is at first situated at the updraught side of the primary vortex close to the wall. The interaction of the primary and secondary vortex leads to 'new three-dimensional vortices which locally initiate the final breakdown . . . '. They further found that the secondary-instability results depend strongly on the amplitude and the higher harmonics of the fundamental crossflow vortex mode. Since it is difficult in a TDNS to keep an initially steady mode steady – not the disturbance frequency but the spatial wavevector is fixed during the computation – detailed clarifying investigations of the secondary instability under well-defined steady vortex conditions were not reported.

SDNS studies by the Stuttgart group (Müller, Bestek & Fasel 1994) clarified some steady–unsteady crossflow mode interactions in the DLR-Göttingen Prinzipexperiment but suffered, like the investigation of the breakdown mechanisms, from a creeping numerical instability that prevented an integration time long enough for the time transients to convect or die out. The problem was identified and later cured by Bonfigli & Kloker (1999, 2000). Then very good agreement was found with the DLR experiment for explosive transition caused by a dominating vortex, and slowly proceeding transition in the case of a dominating single unsteady crossflow wave. The first more detailed SDNS study focusing on the secondary instability of crossflow vortices in a Falkner–Skan–Cooke flow was performed by Högberg & Henningson (1998). They identified the low-frequency mode III and observed it to be amplified much earlier, but also much weaker than the high-frequency 'z' mode, which is amplified 'only

once the crossflow vortices have started to saturate'. They conclude that in a low-noise environment one may expect the high-frequency instability to cause transition, since it has a so much higher growth rate, whereas in a flow with higher levels of free-stream turbulence transition may be caused by the low-frequency mode, since it has its onset further upstream. However, the nonlinear development analysed or state of the primary vortex considered is difficult to reproduce, since the disturbance amplitudes were not clearly set out, and the final stages and flow structures were not captured.

Intensification of secondary-instability work in the presence of steady crossflow vortices occurred with the pioneering ASU experiments on transition delay on their model wing by forcing vortices with subcritical spanwise spacing by artificial roughness (see Saric, Carrillo & Reibert 1998*a*, *b* and White & Saric 2000). Observed nonlinear interactions or mutual suppressions of steady crossflow modes led to the intriguing idea of inducing vortices with a spanwise wavelength smaller than that of the most unstable mode in order to suppress it. For the wing profile considered a delay could indeed be shown. A theoretical analysis by Malik *et al.*, included in their most thorough work on secondary instability (Malik *et al.* 1999), reproduces some of the results. A closer look however reveals that the amplitude drop of the critical vortex mode is unclear (cf. figure 4*e* in their paper) and that the growth, indicated by the N-factor related to e^N-growth of the secondary disturbances, up to the drop point is larger than in the uncontrolled case, despite a lower primary-disturbance amplitude.

The idea of a useful 'upstream flow deformation' by 'non-critical' vortices was also proposed and followed within the project reported here. The project proceeded without knowledge of the successful work of Saric *et al.* until 1998 when the first results were internationally reported; therefore the base flow used differs from the ASU experiments. At that time results of nonlinear saturation states of vortex packets with various initial phase relations and amplitudes of the contained modes were reported, see Wassermann & Kloker (1999, 2000).

Despite the work done on nonlinear saturation and secondary instability of steady crossflow vortices there are important issues still unresolved that are addressed in this paper. 'Clean-conditions' SDNS of a boundary-layer flow with internal disturbance forcing are used to tackle the following issues:

(i) dependence of the secondary instability properties on the spectral content of the primary disturbances;

(ii) examination of the conditions usually invoked for the onset of secondary instability;

(iii) nature of secondary instability: convective or absolute;

(iv) visualization and identification of relevant flow structures during the breakdown stage;

(v) clarification of relevant mechanisms active in the upstream flow deformation technique (in a base flow different from the ASU experiment).

The structure of the paper is as follows: In § 2 the numerical method and the code validation are presented. In §§ 3, 4 and 5 simulation results for the base flow, transition processes and transition delay are discussed, respectively. Throughout the remainder of the paper 'DNS' is taken to mean 'SDNS'.

2. Numerical method

2.1. *Governing equations*

The numerical model is based on the complete three-dimensional Navier–Stokes equations for incompressible unsteady flows in a vorticity–velocity formulation. All

variables are non-dimensionalized by the reference length $\bar{L} = 0.05\,\mathrm{m}$, the chordwise free-stream velocity $\bar{U}_\infty = 30\,\mathrm{m\,s^{-1}}$ and the Reynolds number $Re = \bar{U}_\infty \bar{L}/\bar{\nu} = 100\,000$, where the overbar denotes dimensional variables and $\bar{\nu}$ is the kinematic viscosity:

$$\left.\begin{aligned} x &= \frac{\bar{x}}{\bar{L}}, \quad y = Re^{1/2}\frac{\bar{y}}{\bar{L}}, \quad z = \frac{\bar{z}}{\bar{L}}, \quad t = \frac{\bar{t}\bar{U}_\infty}{\bar{L}}, \quad Re = \frac{\bar{U}_\infty \bar{L}}{\bar{\nu}}, \\ u &= \frac{\bar{u}}{\bar{U}_\infty}, \quad v = Re^{1/2}\frac{\bar{v}}{\bar{U}_\infty}, \quad w = \frac{\bar{w}}{\bar{U}_\infty}, \\ \omega_x &= \frac{\bar{\omega}_x \bar{L}}{\bar{U}_\infty} Re^{-1/2}, \quad \omega_y = \frac{\bar{\omega}_y \bar{L}}{\bar{U}_\infty}, \quad \omega_z = \frac{\bar{\omega}_z \bar{L}}{\bar{U}_\infty} Re^{-1/2}. \end{aligned}\right\} \tag{2.1}$$

With the vectors of vorticity $\boldsymbol{\omega} = \{\omega_x, \omega_y, \omega_z\}^T$ and velocity $\boldsymbol{u} = \{u, v, w\}^T$, where u denotes the velocity in the chordwise (x-), v in the wall-normal (y-) and w in the spanwise (z-) direction, the equations are

$$\frac{\partial \omega_x}{\partial t} + \frac{\partial}{\partial y}(v\omega_x - u\omega_y) - \frac{\partial}{\partial z}(u\omega_z - w\omega_x) = \tilde{\Delta}\omega_x, \tag{2.2a}$$

$$\frac{\partial \omega_y}{\partial t} - \frac{\partial}{\partial x}(v\omega_x - u\omega_y) + \frac{\partial}{\partial z}(w\omega_y - v\omega_z) = \tilde{\Delta}\omega_y, \tag{2.2b}$$

$$\frac{\partial \omega_z}{\partial t} + \frac{\partial}{\partial x}(u\omega_z - w\omega_x) - \frac{\partial}{\partial y}(w\omega_y - v\omega_z) = \tilde{\Delta}\omega_z, \tag{2.2c}$$

$$\frac{\partial^2 u}{\partial x^2} + \frac{\partial^2 u}{\partial z^2} = -\frac{\partial \omega_y}{\partial z} - \frac{\partial^2 v}{\partial x \partial y}, \tag{2.2d}$$

$$\tilde{\Delta} v = \frac{\partial \omega_x}{\partial z} - \frac{\partial \omega_z}{\partial x}, \tag{2.2e}$$

$$\frac{\partial^2 w}{\partial x^2} + \frac{\partial^2 w}{\partial z^2} = \frac{\partial \omega_y}{\partial x} - \frac{\partial^2 v}{\partial y \partial z}, \tag{2.2f}$$

with the modified Laplacian

$$\tilde{\Delta} = \frac{1}{Re}\frac{\partial^2}{\partial x^2} + \frac{\partial^2}{\partial y^2} + \frac{1}{Re}\frac{\partial^2}{\partial z^2}. \tag{2.3}$$

The three vorticity components are defined as

$$\omega_x = \frac{1}{Re}\frac{\partial v}{\partial z} - \frac{\partial w}{\partial y}, \quad \omega_y = \frac{\partial w}{\partial x} - \frac{\partial u}{\partial z}, \quad \omega_z = \frac{\partial u}{\partial y} - \frac{1}{Re}\frac{\partial v}{\partial x}. \tag{2.4}$$

We use a disturbance formulation keeping the full equation set, in order to ease formulation of boundary conditions. Each flow variable is split into the steady laminar base flow part (index B) with $\partial/\partial z \equiv 0$ and the unsteady three-dimensional disturbance flow part (denoted by a prime):

$$f(x, y, z, t) = f_B(x, y) + f'(x, y, z, t) \quad \text{with} \quad f \in \{u, v, w, \omega_x, \omega_y, \omega_z\}. \tag{2.5}$$

Note that for nonlinear disturbances the time mean $\langle f' \rangle \neq 0$ of course. The simulation is carried out in a rectangular integration domain (figure 1). First, the steady base flow is calculated; subsequently, defined disturbances are introduced in disturbance strips at the wall and the disturbance flow is calculated.

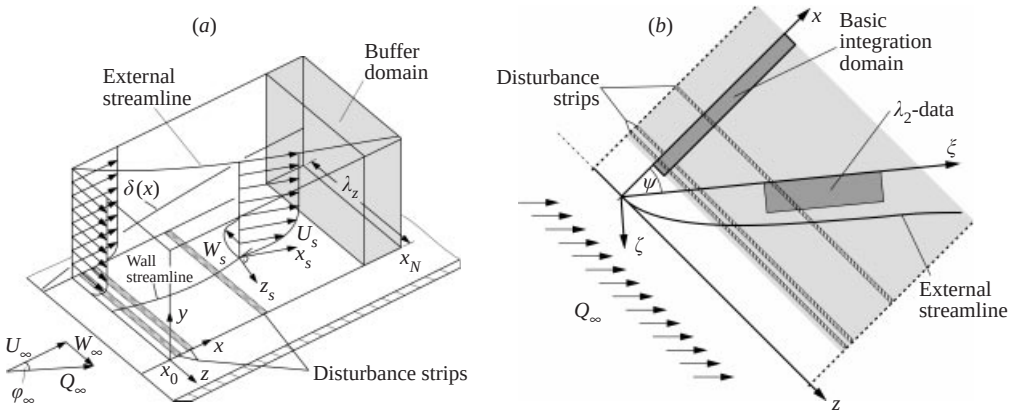

FIGURE 1. (*a*) Integration box. (*b*) Top view of the swept flat plate with the vortex-oriented coordinate system ((ξ, ζ), rotated by $\psi = 39°$ versus the chordwise system).

2.2. *Calculation of the steady laminar base flow*

The calculation of the base flow relies strongly on the assumption of infinite span, i.e. all quantities are independent of the spanwise coordinate z, but there is a velocity component w_B in the spanwise direction. The equations are obtained from (2.2*a*)–(2.2*f*) by neglecting all z-derivatives and are discretized by high-order finite differences. The vorticity equations are solved by a semi-implicit pseudo-temporal technique, and the Poisson equations by a vectorizable stripe-pattern LSOR-technique (iteratively in x-direction).

The boundary conditions are as follows. At the wall ($y = 0$) no-slip and for the vorticity components the following equations are used:

$$\frac{\partial \omega_{x,B}}{\partial x} = -\frac{\partial \omega_{y,B}}{\partial y}, \quad \omega_{y,B} = 0, \quad \frac{\partial \omega_{z,B}}{\partial x} = -\frac{1}{Re}\frac{\partial^2 v_B}{\partial x^2} - \frac{\partial^2 v_B}{\partial y^2}. \tag{2.6}$$

At the inflow boundary ($x = x_0$) a local Falkner–Skan–Cooke solution appropriate to the local $\partial u_e(x)/\partial x$ is used for $u_B(x_0, y)$, $w_B(x_0, y)$, $\omega_{x,B}(x_0, y)$ and $\omega_{z,B}(x_0, y)$, and the remaining quantities $v_B(x_0, y)$ and $\omega_{y,B}(x_0, y)$ are calculated iteratively from the continuity equation and solenoidality of $\boldsymbol{\omega}$, respectively. At the outflow boundary ($x = x_N$) the equations are solved by neglecting the second x-derivatives following usual boundary-layer-theory assumptions, and u_B and w_B are calculated from

$$\frac{\partial^2 u_B}{\partial y^2} = \frac{\partial \omega_{z,B}}{\partial y}, \qquad u_B(x_N, 0) = 0, \quad u_B(x_N, y_M) = u_{B,e}(x_N), \tag{2.7a}$$

$$\frac{\partial^2 w_B}{\partial y^2} = \frac{1}{Re}\frac{\partial \omega_{y,B}}{\partial x} - \frac{\partial \omega_{x,B}}{\partial y}, \quad w_B(x_N, 0) = 0, \quad w_B(x_N, y_M) = W_\infty. \tag{2.7b}$$

At the upper boundary ($y = y_M$) vanishing vorticity and a chordwise-velocity distribution $u_B(x, y_M) = u_{B,e}(x)$ are prescribed. The spanwise velocity component is assumed to be constant $w_B(x, y_M) = W_\infty = U_\infty \tan(\varphi_\infty)$ and the wall-normal velocity component $v_B(x, y_M)$ is obtained from the continuity equation. In this work, $u_e(x)$ at the upper boundary is obtained from the potential velocity distribution $u_{p0}(x)$, valid at $y = 0$ in inviscid flow, by a complex flow function for potential flow. This function is obtained by integrating the analytical distribution $u_{p0}(x)$ (see § 3). Thus,

an effect of the integration-domain height on the actual boundary-layer edge velocity $u_\delta(x)(\approx u_{p0}(x))$ and integral boundary-layer parameters is excluded.

2.3. *Calculation of the unsteady disturbance flow*

The equations for the disturbance quantities are derived from the equations (2.2*a*)–(2.2*f*) with the decomposition (2.5) leaving out the zero sum of all pure base-flow terms. The assumption of infinite span yields periodic boundary conditions in the spanwise direction. Thus, the numerical method uses a complex Fourier spectral representation to calculate the non-symmetric three-dimensional flow. All variables are decomposed as

$$f'(x,y,z,t) = \sum_{k=-K}^{K} \hat{f}_k(x,y,t)\mathrm{e}^{\mathrm{i}k\gamma z} \quad \text{with} \quad \gamma = \frac{2\pi}{\lambda_z},\ \mathrm{i}^2 = -1,\ \hat{f}_k \in \mathbb{C}, \tag{2.8}$$

where γ is the basic spanwise wavenumber. The $\hat{f}_{-k}$ are the complex conjugates of the $\hat{f}_k$ and do not have to be computed, but for $\hat{f}_k$ both the real and imaginary parts of the equations have to be solved thus doubling the computational effort compared to a three-dimensional symmetric flow field. With this decomposition we obtain a system of $K+1$ complex two-dimensional differential equations coupled by the nonlinear terms, which are represented by $\hat{X}_k$, $\hat{Y}_k$ and $\hat{Z}_k$. Thus,

$$\frac{\partial \hat{\omega}_{x,k}}{\partial t} + \hat{X}_k = \tilde{\Delta}_k \hat{\omega}_{x,k}, \tag{2.9a}$$

$$\frac{\partial \hat{\omega}_{y,k}}{\partial t} + \hat{Y}_k = \tilde{\Delta}_k \hat{\omega}_{y,k}, \tag{2.9b}$$

$$\frac{\partial \hat{\omega}_{z,k}}{\partial t} + \hat{Z}_k = \tilde{\Delta}_k \hat{\omega}_{z,k}. \tag{2.9c}$$

The modified spectral Laplacian $\tilde{\Delta}_k$ is

$$\tilde{\Delta}_k = \frac{1}{Re}\frac{\partial^2}{\partial x^2} + \frac{\partial^2}{\partial y^2} - \frac{(k\gamma)^2}{Re}. \tag{2.10}$$

The Poisson-type equations for the velocity components are

$$\frac{\partial^2 \hat{u}_k}{\partial x^2} - (k\gamma)^2 \hat{u}_k = -\mathrm{i}k\gamma\hat{\omega}_{y,k} - \frac{\partial^2 \hat{v}_k}{\partial x \partial y}, \qquad k \neq 0, \tag{2.11a}$$

$$\frac{\partial \hat{u}_0}{\partial x} = -\frac{\partial \hat{v}_0}{\partial y}, \qquad k = 0, \tag{2.11b}$$

$$\tilde{\Delta}_k \hat{v}_k = \mathrm{i}k\gamma\hat{\omega}_{x,k} - \frac{\partial \hat{\omega}_{z,k}}{\partial x}, \qquad \forall k, \tag{2.11c}$$

$$\frac{\partial^2 \hat{w}_k}{\partial x^2} - (k\gamma)^2 \hat{w}_k = \frac{\partial \hat{\omega}_{y,k}}{\partial x} - \mathrm{i}k\gamma\frac{\partial \hat{v}_k}{\partial y}, \qquad k \neq 0, \tag{2.11d}$$

$$\frac{\partial \hat{w}_0}{\partial x} = -\hat{\omega}_{y,0}, \qquad k = 0. \tag{2.11e}$$

The boundary conditions are as follows. At the upper boundary ($y = y_m$) potential flow holds:

$$\omega'_x = \omega'_y = \omega'_z = 0. \tag{2.12}$$

For v', the local wall-normal gradient is prescribed:

$$\frac{\partial v'}{\partial y} = -\alpha^* Re^{-1/2} v', \tag{2.13}$$

where α^* can be thought of as a streamwise wavenumber of the disturbance (cf. linear stability theory). Numerical experience shows that the value of α^* is not crucial and may also be set to zero. At the inflow boundary all disturbance quantities are set to zero, except when a previous simulation is continued with a downstream-shifted inflow boundary (see § 2.4). At the wall the no-slip condition is satisfied for u' and w'. Also the velocity v' is zero at the wall, except in the disturbance strips ($x \in [x_j - 0.5\Delta x_s, x_j + 0.5\Delta x_s]$; typically $\Delta x_s = 14\Delta x$). There the disturbances are enforced with momentum input but no net mass flow:

$$v'(x,y,z,t) = f_v(x)\left(\sum_{k=1}^{K} 2A_{0,k}\cos(k\gamma z + \Theta_{0,k}) + \sum_{h=1}^{H}\sum_{k=-K}^{K} 2A_{h,k}\cos(k\gamma z - h\beta t + \Theta_{h,k})\right); \tag{2.14}$$

f_v is a piecewise-defined symmetric fourth-order parabola ($-3\tau^4 + 4\tau^3$ for $0 \leqslant \tau < 1$, and $-3(2-\tau)^4 + 4(2-\tau)^3$ for $1 \leqslant \tau \leqslant 2$, $[0,2] \mapsto [x_j - 0.5\Delta x_s, x_j + 0.5\Delta x_s]$, cf. top insert in figure 6); it has vanishing first and second derivatives at the respective ends of the strips. In the time direction the disturbance function is smoothly turned on with an envelope curve. The vorticity components at the wall are computed by solving the following equations:

$$\frac{\partial \hat{\omega}'_{x,k}}{\partial x} = -\frac{\partial \hat{\omega}'_{y,k}}{\partial y}, \qquad \hat{\omega}'_{x,k}\Big|_{x_0} = 0, \qquad k = 0, \tag{2.15a}$$

$$\frac{\partial^2 \hat{\omega}'_{x,k}}{\partial x^2} - (k\gamma)^2 \hat{\omega}'_{x,k} = -\frac{\partial^2 \hat{\omega}'_{y,k}}{\partial x \partial y} + \mathrm{i}k\gamma\tilde{\Delta}\hat{v}'_k, \quad \hat{\omega}'_{x,k}\Big|_{x_0} = 0, \frac{\partial^2 \hat{\omega}'_{x,k}}{\partial x^2}\Big|_{x_N} = 0, \quad k \neq 0, \tag{2.15b}$$

$$\hat{\omega}'_{y,k} = 0, \qquad \forall k \tag{2.15c}$$

$$\frac{\partial \hat{\omega}'_{z,k}}{\partial x} = \mathrm{i}k\gamma\hat{\omega}'_{x,k} - \tilde{\Delta}\hat{v}'_k, \qquad \hat{\omega}'_{z,k}\Big|_{x_0} = 0, \qquad \forall k, \tag{2.15d}$$

where the subscripts x_0 and x_N indicate boundary conditions to be set at the inflow and at the outflow, respectively.

For the outflow boundary, a self-developed and well-tested damping-zone technique is applied, wherein the vorticity disturbance vector is directly forced to zero upstream of the actual outflow boundary (see Kloker, Konzelmann & Fasel 1993 for non-skew base flow, and Bonfigli & Kloker 1999 for skew base flow). Within the first, say, 2/3 of the chordwise damping-zone extent the damping function falls from one to zero, and stays zero within the remainder. In the case of a skew base flow it is crucial to satisfy the solenoidality of $\boldsymbol{\omega}$ for the two-dimensional Fourier component $k = 0$ in the damping zone, which is identically satisfied in the case of non-skew base flow. Therefore, here only the chordwise and spanwise vorticity components are forced to zero for $k = 0$, while the wall-normal component is computed (for further details see Bonfigli & Kloker 1999). The actual boundary conditions are of minor relevance as long as they do not disagree with the required decay of the disturbance amplitudes. In the present implementation, all second x-derivatives are locally set to zero at the outflow; this translates into $\hat{v}'_k \equiv 0$ at the outflow. To solve the equations for $\hat{u}_k$ and $\hat{w}_k$, $k \neq 0$, we need a Dirichlet condition at the outflow that can be obtained by

integrating locally the vorticity definitions:

$$\frac{\partial \hat{u}'_k}{\partial y} = \hat{\omega}'_{z,k} + \frac{1}{Re}\frac{\partial \hat{v}'_k}{\partial x}, \qquad \hat{u}'_k\Big|_{y=0} = 0, \qquad k \neq 0, \tag{2.16a}$$

$$\frac{\partial \hat{w}'_k}{\partial y} = -\hat{\omega}'_{x,k} + \frac{ik\gamma}{Re}\hat{v}'_k, \qquad \hat{w}'_k\Big|_{y=0} = 0, \qquad k \neq 0. \tag{2.16b}$$

In the x- and y-directions, a finite-difference (FD) discretization is used, based on a blockwise equidistant rectangular grid with a special wall zone, where the step size Δy is halved. Principally, sixth-order compact FDs are used. The nonlinear terms in the vorticity transport equations are computed pseudospectrally and their x-derivatives are differenced with a special split-type method with inherent damping; the time integration is done by a 4-step fourth-order Runge–Kutta method. For a thorough numerical analysis of the used FD discretization and the time stepping scheme see Kloker (1998).

The computation of each Runge–Kutta step starts with the explicit computation of $\boldsymbol{\omega}$ in the whole domain except at the wall. Thereafter the new vorticity distribution, with the exception of the spectral component $\hat{\omega}_{y,0}$, is forced to zero within the damping zone. The wall-normal velocity v' is computed by solving (2.11c), and the vorticity components ω'_x and ω'_z are evaluated at the wall by integrating equations (2.15a)–(2.15d) and thereafter superimposing the damping function. Finally, u' and w' are computed by solving equations (2.11a, b) and (2.11d, e) with prior calculation of the Dirichlet conditions for $k > 0$ using (2.16a, b).

2.4. *Code validation and numerical parameters*

The numerical method presented above has been carefully verified and validated for several scenarios in two- and three-dimensional base flows and yielded good agreement with experimental data or theoretical (linear stability theory, PSE) calculations. In the case of three-dimensional base flow in particular the results have been successfully validated for the canonical crossflow-transition experiment at DLR Göttingen (see Bonfigli & Kloker 1999, 2000; figure 7 in Koch *et al.* 2000). For the base flow presented here we have compared the quasi-linear development of small-amplitude steady crossflow modes with results of Spalart, Crouch & Ng (1994). The chordwise amplitude developments shown in figure 2 for two spanwise wavenumbers are in very good agreement.

The spanwise Fourier ansatz principally reduces the three-dimensional problem in physical space to a (coupled) set of $(K + 1)$ complex two-dimensional problems in Fourier space thus enabling a largely parallel computation in Fourier space. However, the modes are coupled by the nonlinear convective terms of the vorticity transport equations and are transformed to physical space for the calculation of the nonlinear terms, which in turn are parallelized in the streamwise direction. This pseudospectral method is employed with de-aliasing, $4K$ points were used in spanwise direction.

For the following simulations the uniform equidistant grid typically contained $2106 \times 257 \times 64$ ($K = 16$) points in the (x, y, z)-directions. It is noted that the y-discretization, especially in the near-wall region, is the crucial point in resolution requirements. For the first 33 points in the wall-normal direction $\Delta y_{wz} = \Delta y/2$. The number of time steps per fundamental disturbance period $\beta = 2\pi \bar{f} \bar{L}/\bar{U}_\infty = 10$ was 1600. For the fine-resolution simulation (Case 2B-f) we used a $2610 \times 385 \times 256$ ($K = 62$) grid. The inflow boundary had been shifted downstream from $x_0 = 0.25$ to $x_0 = 1.68$ in this case, using steady boundary conditions for all disturbance variables

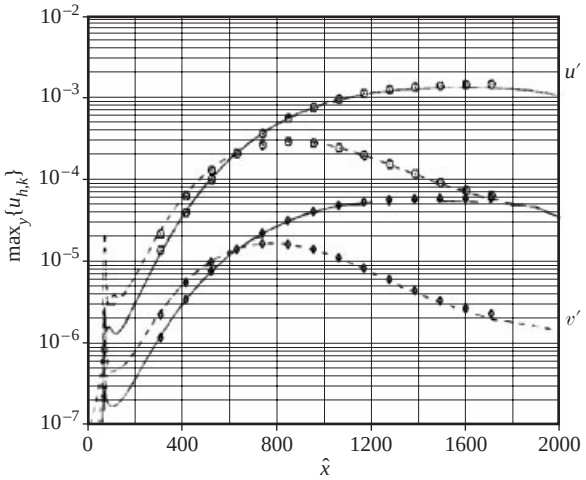

FIGURE 2. Comparison of chordwise amplitude development for two crossflow vortex modes with results of Spalart *et al.* (1994). The curves show the $u'_{(0,1)}$ and $v'_{(0,1)}$ amplitude development for steady crossflow vortex modes with $\gamma = 125$ (upper) and $\gamma = 167$ (lower), as scanned from their paper, figure 3. Our DNS results are marked by the symbols. Here $\hat{x} = 400x$; $\gamma = \bar{\gamma}\bar{L}$. The respective u'-amplitude curves are fit near $\hat{x} \approx 300$, with the ratio u'/v' untouched.

in the second run directly at the inflow boundary extracted from the first computation within the domain by a timewise Fourier decomposition. Thus the number of grid points in the x-direction could be kept almost constant despite the finer discretization. All relevant simulation parameters are summarized in table 1. This run clearly showed that the typical grid used with $K = 16$ is fine enough to correctly capture the flow physics discussed. A direct comparison can be drawn from figures 13 ($K = 16, \Delta x, \Delta y$) and 11 ($K = 62, \frac{1}{2}\Delta x, \frac{2}{3}\Delta y$). In nonlinear PSE computations also typically 12–16 spanwise modes are considered to be sufficient. Wintergerste & Kleiser (1997) found in their TDNS that at least 80 'spanwise' modes are necessary for a saturated vortex. We point out that this is not consistent with the SDNS or PSE findings and that they use a coordinate system aligned with the vortex.

The problem has been run on the NEC SX-4/32 (32 processors, 8 GB RAM) and the NEC SX-5 (16 processors, 32 GB RAM) of the high-performance computing centre Stuttgart (HLRS). A calculation on the NEC SX-5/16 takes about 2.2 µs per grid point and full time step on a single processor. The memory requirement is about 150 Bytes per point, depending on the included online data processing.

3. Laminar base flow

The base flow is designed to resemble the flow in the front region of a swept wing. The streamwise edge velocity is taken from Spalart *et al.* (1994) and defined analytically by

$$u_{p0}(x) = \frac{3}{2\pi}\left(\arctan\left(\frac{x-a}{b}\right) + \arctan\left(\frac{x+a}{b}\right)\right) - cx, \tag{3.1}$$

with

$$a = 0.2611, \quad b = 0.41015, \quad c = 0.056.$$

The integration domain starts at $x_0 = 0.25$ close to the leading edge (local Hartree

	Primary disturbances at $x = x_2 = 0.68$ (for Case 4/4B at $x = x_1 = 0.57$)		
Case	Modes	Amplitudes $A_{(h,k)}$	Phases $\Theta_{(h,k)}$
1	(0,1) – (0,4)	1.0×10^{-7}	0
2/2B	(0,1) – (0,4)	0.005	$(k-1)\pi$
2B-f	(0,1) – (0,4)	0.005	$(k-1)\pi$
2WP	(0,1) – (0,4)	0.005	$(k-1)\pi$
	(1,±1) – (1,±4)	0.001	$(k-1)\pi$
3/3B	(0,2)	0.005	0
4/4B	(0,3)	0.02	0
5/5B	(0,1) – (0,4)	0.005	$(k-1)\pi$
6/6B	(0,1) – (0,4)	0.005	$(k-1)\pi$
7	(0,1) – (0,4)	0.005	$(k-1)\pi$

	Upstream flow deformation by mode (0,3) at $x = x_1 = 0.57$		Periodic background pulses (B) at $x_3 = 2.0$: $h = 1-30$, $\beta = 10$	
Case	Amplitude $A_{(0,3)}$	Phase $\Theta_{(0,3)}$	Modes	Amplitudes $A_{(h,k)}$
1	—	—	—	—
2/2B	—	—	$(h, \pm 2)$	5.0×10^{-5}
2B-f	—	—	$(h, \pm 2)$	5.0×10^{-5}
2WP	—	—	—	—
3/3B	—	—	$(h, \pm 2)$	5.0×10^{-5}
4/4B	—	—	$(h, \pm 3)$	5.0×10^{-5}
5/5B	0.02	0	$(h, \pm 2)$	5.0×10^{-5}
6/6B	0.05	0	$(h, \pm 2)$	5.0×10^{-5}
7	(0,0) extracted from Case 6		—	—

	Computational parameters			
Case	Comp. basic wavenumber γ_c	Spanwise resolution K	Δx	Δy
1	45	4	0.0017952	0.088016
2/2B	45	16	0.0017952	0.088016
2B-f	45	62	0.0008976	0.058677
2WP	45	16	0.0017952	0.088016
3/3B	90	8	0.0017952	0.088016
4/4B	135	8	0.0017952	0.088016
5/5B	45	16	0.0017952	0.088016
6/6B	45	16	0.0017952	0.088016
7	45	16	0.0017952	0.088016

TABLE 1. Simulation parameters for the calculations presented. The computational grid typically contains 2106×257 points in the (x, y)-direction and the inflow boundary is at $x_0 = 0.25$. For Case 2B-f 2610×385 points have been used and the inflow was at $x_0 = 1.68$. Note that for the first 33 points in the wall-normal direction $\Delta y_{wz} = \Delta y/2$. For the spanwise resolution K denotes the number of de-aliased spectral modes and therefore $\Delta z = 2\pi/(4\gamma_c K)$. The letter 'B' denotes that the background pulses are superimposed.

$\beta_H(x_0) = 0.99$) and extends for the following investigations to $x_N = 4.03$. The sweep angle is $\varphi_\infty = 45°$ and the local angle of the external streamline varies from $\varphi_e(x_0) = 68.1°$ to the minimum value of $\varphi_e = 39.7°$ at $x = 2.65$, and $\varphi_e(x_N) = 40.3°$. The Reynolds number based on the chordwise displacement thickness δ_1 rises from $Re_{\delta 1}(x_0) = 67$ to $Re_{\delta 1}(x_N) = 1180$ and the displacement thickness increases by a factor of six within the domain. The crossflow amplitude $\tilde{w}_{s,B} = w_{s,B}/u_{s,B,e}$ decreases

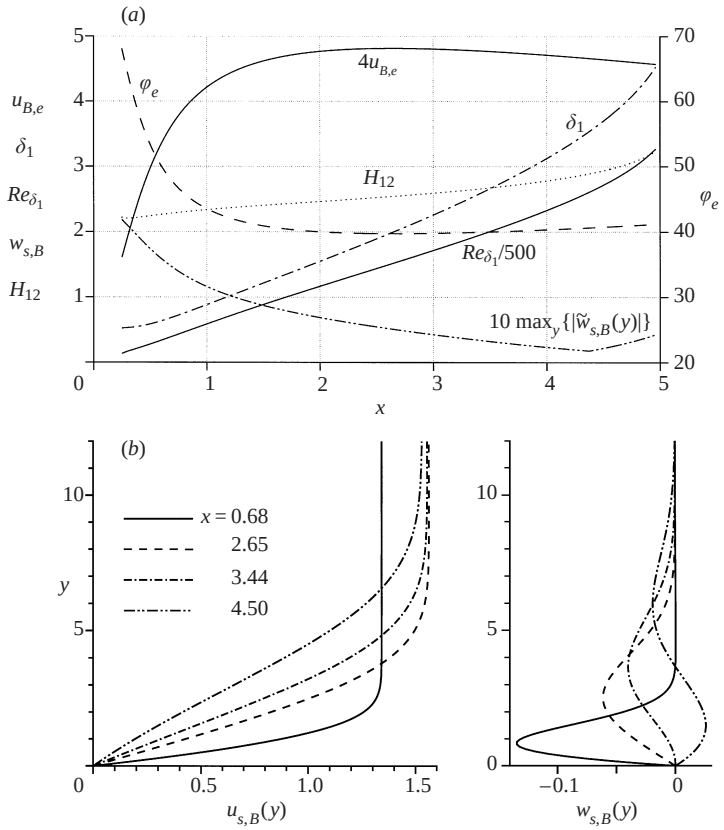

FIGURE 3. (*a*) Base flow parameters in the plate-fixed coordinate system. (*b*) Mean-flow and crossflow profiles at various downstream positions.

from 10% to 5% in the relevant region, and for $x \geqslant 3.5$ the crossflow profiles $w_{s,B}(y)$ are S-shaped (see figure 3).

4. Breakdown of saturated crossflow vortices

4.1. *Primary growth and nonlinear saturation of a crossflow-vortex-mode packet*

First, the base flow was analysed by means of spatial linear stability theory (LST) to obtain an overview of relevant instability modes (figure 4). As a result, the fundamental spanwise wavenumber $\gamma_1 = 45$ ($= \bar{\gamma}_1 \bar{L}$) has been chosen for the subsequent DNS of a packet of steady modes $(0,k)$, $k = 1$–4, introduced in the disturbance simulation by imposing a steady wall-normal velocity distribution within the disturbance strip at the wall. In this way, it is possible to consider the locally most amplified as well as the integrally most amplified steady crossflow vortex mode and their later nonlinear interaction. The discrete waves are presented in the frequency–spanwise wavenumber spectrum (h,k), so the mode $(0,k)$ denotes a stationary mode with the spanwise wavenumber $k\gamma_1$. The most important parameters of all simulation cases discussed in this paper are listed in table 1.

In Case 1 the crossflow-vortex-mode packet is forced at $x_2 = 0.68$ with a small amplitude, $A_{(0,k)} = 1.0 \times 10^{-7} Re^{1/2}$ for $k = 1$–4, and its quasi-linear downstream development was computed to study the disturbance growth and the propagating

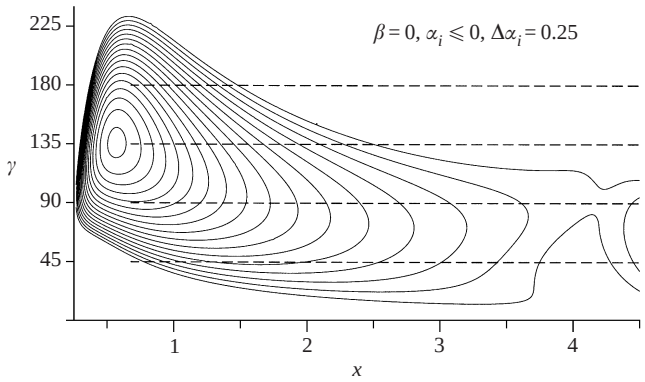

FIGURE 4. Stability diagram for steady crossflow vortex modes from LST; $\alpha_i = \bar{\alpha}_i \bar{L} = 1/A \times \mathrm{d}A/\mathrm{d}x$ (spatial amplification rate). The modes considered in the DNS later on are marked by the dashed lines.

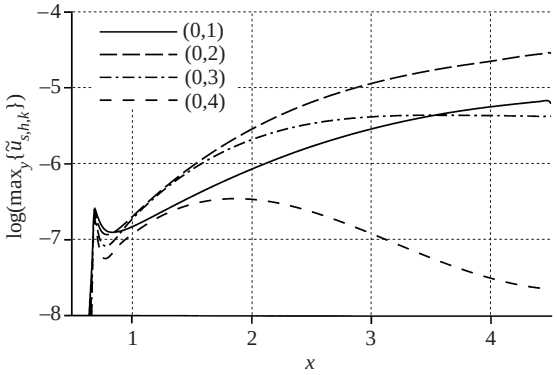

FIGURE 5. Quasi-linear downstream (t-z)-modal amplitude development of the crossflow-vortex-mode packet (Case 1); $\tilde{u}_{s,h,k}$-maximum over y, $\tilde{u}_s = u_s/u_{s,B,e}$

direction. In figure 5 it can be observed that all crossflow vortex modes are strongly amplified first and that the modes (0,1) and (0,2) are growing throughout the whole domain, the mode (0,2) attaining the largest amplitude. The mode (0,3) behaves nearly neutrally downstream, while only the mode (0,4) is damped. The amplification rates are larger than predicted by LST throughout the whole domain; up to $x = 2.65$, a typical amplitude difference of factor $3 \sim 4$ between DNS and LST integration results. The directions of the vortex-mode axes are roughly congruent with the mean-flow direction (for more details see Wassermann & Kloker 1999).

For the calculation of a nonlinear, saturated crossflow-vortex scenario the crossflow vortex-mode packet is introduced with an amplitude of $A_{(0,k)} = 5.0 \times 10^{-3} Re^{1/2}$. The spanwise phase of each mode is chosen in order to model a point-like perturbation. For Case 2, a localized disturbance with momentum, but no net-mass-flow input, is modelled by $\Theta_{(0,k)} = (k-1)\pi$, see the insert in figure 6. This corresponds to a spanwise roughness row with a spacing of twice the most amplified wavelength. By turning on the disturbance, a moving disturbance front is generated, and the flow field settles slowly to a steady state when the front end of the vortex modes reaches the outflow. The t-z-modal Fourier analysis shows that the disturbance components are strongly amplified first by primary instability and saturate with different amplitudes (figure 6).

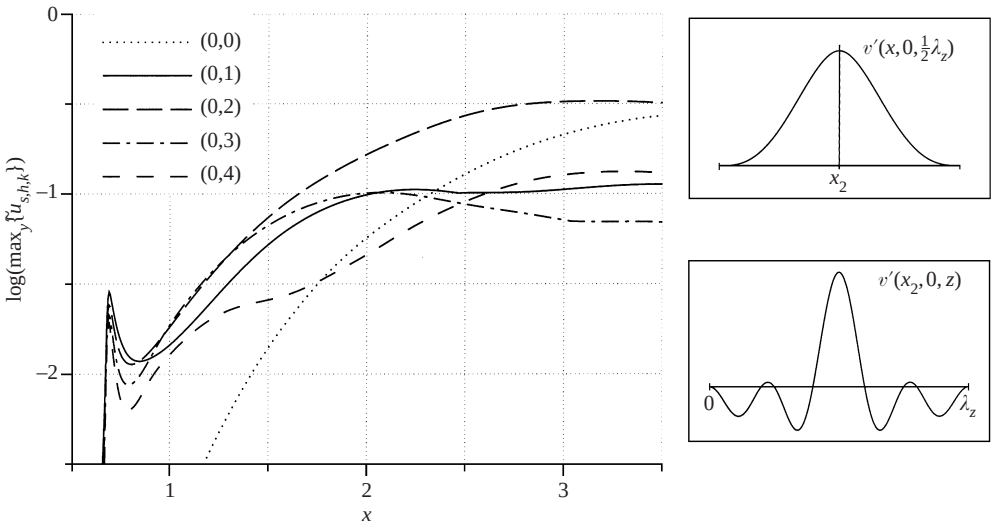

FIGURE 6. Downstream (t-z)-modal amplitude development of the crossflow-vortex-mode packet, Case 2; $\tilde{u}_{s,h,k}$-maximum over y, $\tilde{u}_s = u_s/u_{s,B,e}$. Inserts: chordwise (top) and spanwise (bottom) distribution of the forcing v'-velocity in the disturbance strip. The chordwise extent of the strip typically is $14\Delta x$.

The mode (0,2) attains the highest amplitude and clearly dominates by eventually suppressing the growth of modes (0,1) and (0,3). Accordingly, two streamwise vortices per spanwise wavelength establish with clockwise rotation when looking downstream. Due to the superposition by the other crossflow vortex modes, especially the odd-k modes, one of the vortices is stronger and further away from the wall (see figure 7, $\zeta \approx 0.11$). The vortices transport slow fluid from the near-wall region up into faster regions resulting in a strong steady deformation of the mean-flow profiles $u_s(y)$, $u_s(z)$ with relatively large y- and z-gradients.

4.2. *Secondary instability and laminar breakdown initiated by the crossflow-vortex-mode packet*

In the scenario discussed so far only a steady disturbance input has been considered and the flow field, calculated by a time-accurate time-stepping scheme, finally settled to a steady nonlinear disturbance state. Naturally, transition to turbulence can only be caused by unsteady disturbances. In low-turbulence background conditions a sudden breakdown of the dominating crossflow vortices is observed and the question arises whether this phenomenon is caused by a strong convective or an absolute instability with respect to unsteady modes. 'Absolute' means that a disturbance is amplified in time while remaining principally (with zero group velocity) at a fixed location in space, inevitably causing a nonlinear disturbance state, like e.g. in a bluff-body wake. To date there are experimental investigations (see the reviews Bippes 1997 and Reibert & Saric 1997), investigations with temporal stability analysis (see Koch *et al.* 2000 and Malik *et al.* 1999) and a first spatial DNS study (see Högberg & Henningson 1998) on this issue, but the discussion on whether or not the observed sudden strong instability is of absolute nature is still underway.

For clarification, in Case 2B the saturated crossflow vortex packet has been combined with periodically pulsed low-amplitude disturbances to simulate the natural

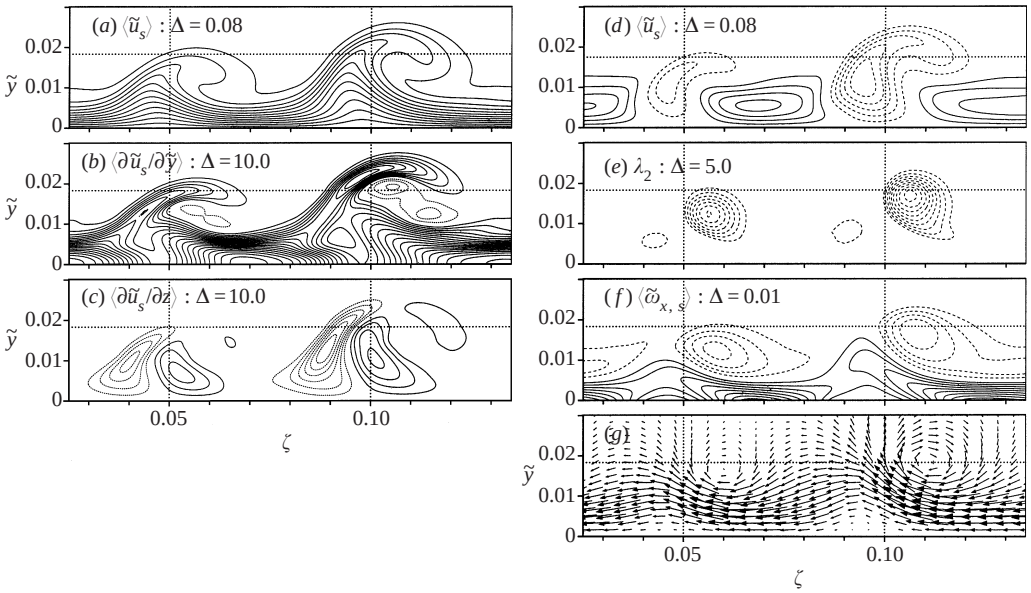

FIGURE 7. Flow field distorted by the nonlinearly saturated crossflow-vortex-mode packet (Case 2) in a crosscut in the vortex-oriented system at $\xi = 3.2$ ($\zeta = 0.05 \rightarrow x = 2.455$): (*a*) deformed mean flow; (*b*,*c*) *y*- and *z*-gradient of the deformed mean flow; (*d*) deformation of the mean flow; (*e*) λ_2 isolines (indicating local pressure minima, see Jeong & Hussain 1995); (*f*) vorticity component in the mean-flow direction; (*g*) velocity vectors (w_s, v). Positive isolines are solid, negative isolines are dashed. The zero line is not shown. Approximately one fundamental spanwise wavelength is shown. To scale ($\tilde{y} = yRe^{-1/2}$). The dotted horizontal line marks the laminar boundary-layer thickness at $\zeta = 0.1$. This quantity varies only by 2% over the ζ-range shown here.

disturbance background. The periodic background pulse, consisting of harmonic waves with discrete frequencies from $\beta = 10$ up to $\beta = 300$ ($\Delta\beta = 10$) for $k = \pm 2$ with $A_{(h,\pm 2)} = 5.0 \times 10^{-5} Re^{1/2}$ for each component, has been excited at $x_3 = 2.0$, just upstream of the crossflow vortex packet's saturation point. For primary instability, the most amplified crossflow mode has $\beta = 14$. The periodic background pulse is only given for the spectral component $k = \pm 2$ since the large-amplitude vortex modes $(0, k)$ generate the other spectral components at once. Note that in what follows mainly a *t*-modal representation of the downstream amplitude development is used since the secondary instabilities are clearly characterized by their two-dimensional (y, z) amplitude distribution and the downstream development of the amplitude maximum (over *y* and *z*) rather than the β-γ-spectral content. After a short transient region the background disturbances undergo strong amplification, especially the component $\beta = 160$, which attains the largest amplitude in this region (figure 8). This mode grows over the smaller frequency modes, although its receptivity is smaller. The maximum spatial amplification rate is three times the maximum primary amplification of the most unstable crossflow mode. The visible growth of the lower as well as the higher frequency modes is clearly nonlinearly generated. Recall that modes (h_1, k_1) and (h_2, k_2) generate modes $(h_1 \pm h_2, k_1 \pm k_2)$.

Isocontours of the $\tilde{u}_s$-amplitude for $\beta = 20$ and $\beta = 160$ in the crosscut corresponding to figure 7 reveal the origin of the secondary instability (figure 9). For the high-frequency (HF) instability the location of the largest amplitude coincides perfectly with the minimum of the spanwise gradient of the time-averaged mean-flow

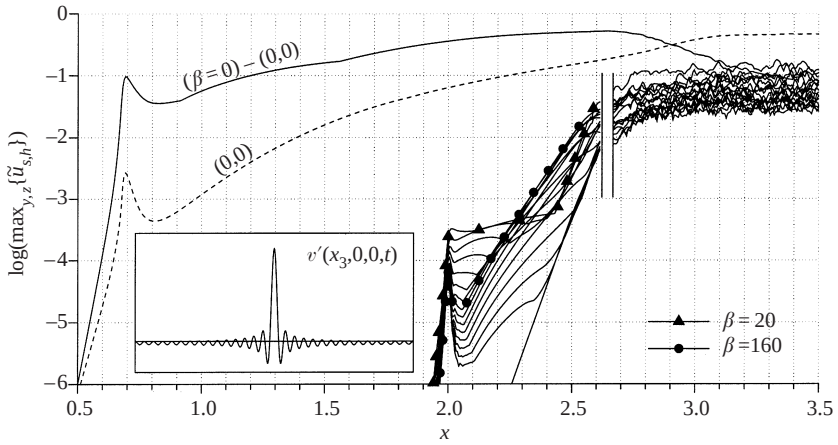

FIGURE 8. Downstream t-modal amplitude development for Case 2B: crossflow-vortex-mode packet plus periodic background pulses. Frequencies from $\beta = 0$ to $\beta = 320$, $\Delta\beta = 20$ are shown. The curves to the left of the two vertical lines are obtained from second time-derivative analysis. The curve denoted by (0,0) represents the two-dimensional part of the mean-flow distortion, and the curve denoted by $(\beta = 0) - (0,0)$ represents the three-dimensional part of it. Insert: time-dependence of the forcing v'-velocity in the centre ($x = x_3, z = 0, -T/2 \leqslant t \leqslant T/2$) of the downstream disturbance strip.

velocity component, see figure 7(c), $\zeta \approx 0.089$, and figure 10(a), with steepest descent of the thick line at the same ζ. Note that it does not really coincide with the region of the most deformed mean profiles at $\zeta \approx 0.11$ (dotted curve in figure 10b) or the maximum wall-normal gradient at $\zeta = 0.097$ (figure 7). Hence, this secondary instability mode corresponds to a 'z' mode, which has been found and named using secondary stability analysis by Malik *et al.* (1999). The mean profile connected to the initiation point of the HF instability is deformed rather weakly, and thus this criterion often invoked for two-dimensional flows obviously fails. A different picture arises for the low-frequency (LF) secondary instability. Exactly at the ξ-position shown here ($\xi = 3.2$, $\zeta = 0.09$ corresponds to $x = 2.43$) a kink can be observed in the amplitude-curve in figure 8 indicating a change of the dominating local amplitude maximum. In figure 9 two distinct maxima appear at $\zeta = 0.051$ and $\zeta = 0.087$. The first is coupled to a local maximum of the spanwise gradient, and the second one obviously arises from nonlinear generation by the HF instability modes; it becomes dominant downstream. Thus from the disturbance shape the energy feedback effect from higher to lower frequency modes can be identified.

The downstream amplification and spreading of the background wave packet in physical space is visualized in figure 11 by means of 'λ_2' isosurfaces which identify vortical structures (by locating a pressure minimum in a plane, see Jeong & Hussain 1995). The background disturbance input is at $\xi \approx 2.65$, just upstream of the shown domain. At $t/T = 0.5$ the pulse disturbance is visible for the first time at $\xi \approx 3.05$, in between the primary vortical structures. At $t/T = 0.75$ a cascade of three small finger-like vortices twining around the left, updraught side of the dominant crossflow vortex emerges at $\xi \approx 3.2$, with their axes aligned at 20° to the crossflow vortex (note the compression of the ξ-axis). On travelling downstream an increasing number of 'finger' vortices appear with continuing disturbance spreading ($t/T = 0, 0.25$). The secondary vortices are much stronger than the primary vortical motion, indicated by a λ_2 value that is a factor of about 50 larger, and by a $\omega_{x,s}$ value that is a

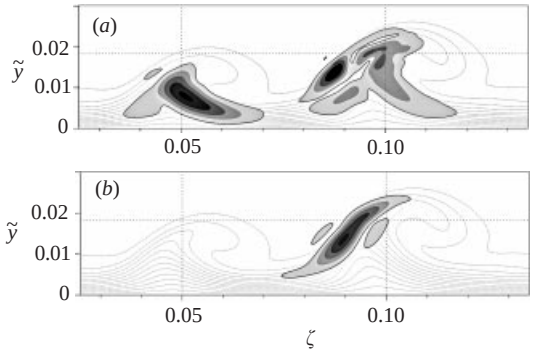

FIGURE 9. Isocontours of normalized $\tilde{u}_{s,h}$-amplitude for $\beta = 20$ (a) and $\beta = 160$ (b) for Case 2B in a crosscut at $\xi = 3.2$. Isolines from 0.15 to 0.95 with a 0.2 spacing are shown and the deformed mean flow is indicated by the dotted lines. To scale ($\tilde{y} = yRe^{-1/2}$).

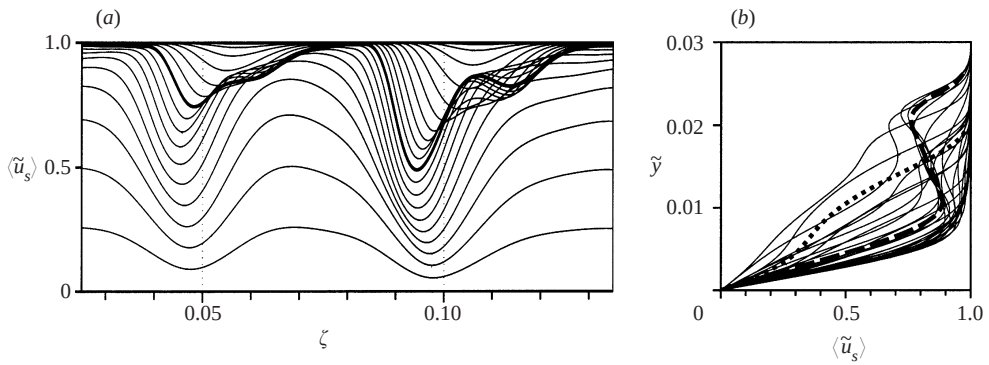

FIGURE 10. Mean-flow profiles $\tilde{u}_s(\zeta)$ and $\tilde{u}_s(y)$ at $\xi = 3.2$ for Case 2: (a) spanwise profiles at equidistant y-positions, the profile for $\tilde{y} = 0.0139$ is emphasized; (b) wall-normal profiles at equidistant ζ-positions, the profiles for $\zeta = 0.09$ (dots) and $\zeta = 0.11$ (dashes) are emphasized.

factor of 7 larger (absolute values). These structures are reminiscent of the 'rib-like' structures constructed in rotating-disk flow by Balachandar, Streett & Malik (1992). Using results of primary and secondary stability theory they obtained pairs of counter-rotating secondary vortices inclined at an angle of 44° to the axis of the primary crossflow vortices. In contrast, the secondary vortices here are co-rotating, in the opposite direction than the primary vortex, and the inclination is significantly smaller. The finger vortices have their roots near the wall but are not connected to the weak steady secondary vortex that lies close to the wall at the updraught side of the strong primary vortex. (This vortex is visible in figure 7*e*, but not in figure 11 with the iso-surface value shown there. We find this steady secondary vortex to be of rather small relevance here; it is just a dynamical consequence of the wave-like fluid motion in the spanwise direction (cf. figure 7*g*) resulting from the superposition of the crossflow and the fluid motion induced by the co-rotating crossflow vortices.) The primary vortex is only weakly modulated by the travelling finger vortices and is mainly persistent. The weaker primary vortex to the left is also modulated by the spreading of the travelling structure, but the visible 'fine scale dust' seems caused by insufficient numerical resolution. Clearly, for the full resolution of the onset of turbulence a higher resolution is necessary. The large-scale structures however are basically not affected, cf. figure 13 ($K = 16, \Delta x, \Delta y$) with figure 11 ($K = 62, \frac{1}{2}\Delta x, \frac{2}{3}\Delta y$).

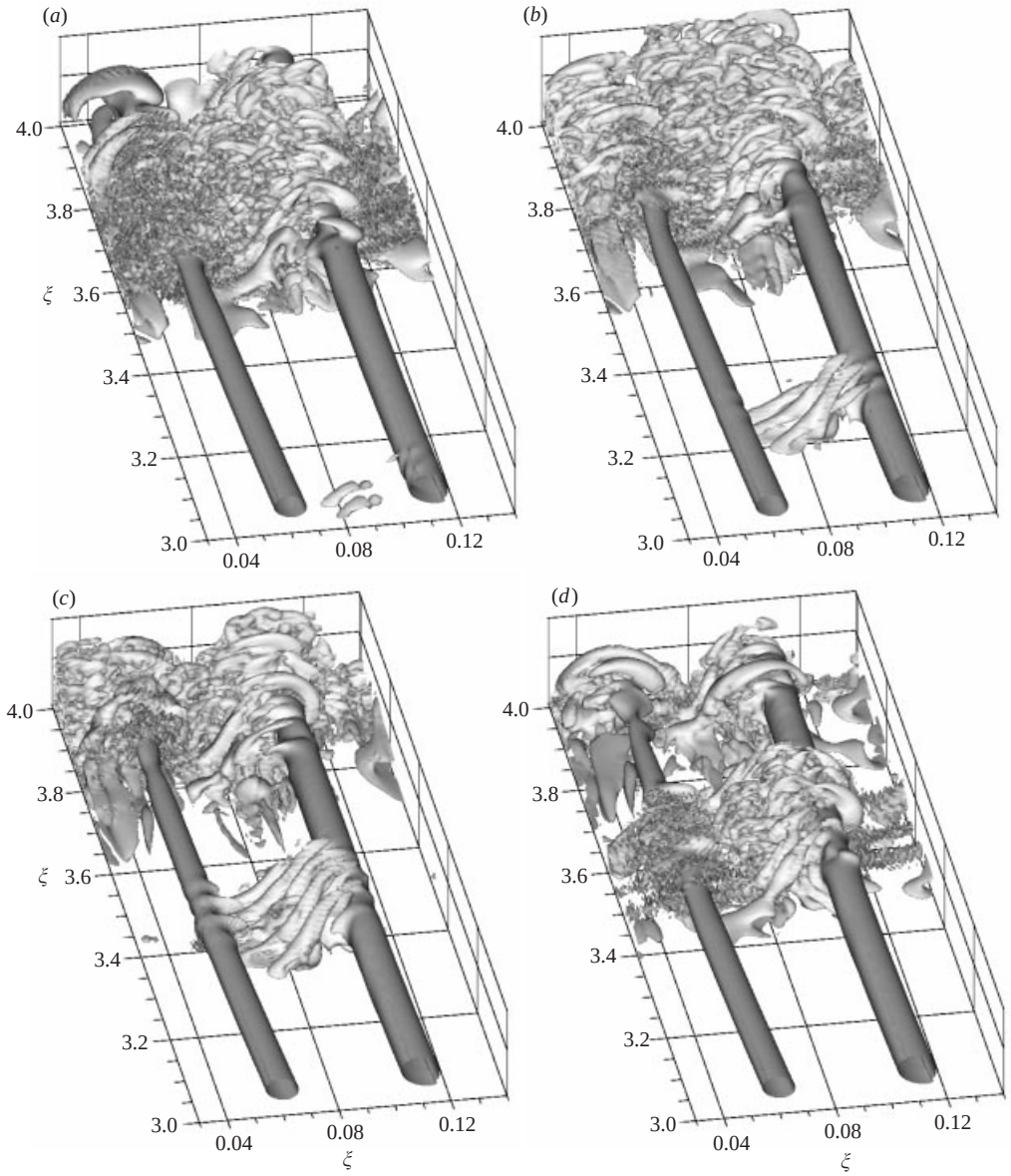

FIGURE 11. Visualization of vortical structures in the instantaneous flow fields for Case 2B-f, crossflow-vortex-mode packet plus periodic background pulses, fine resolution, by λ_2-isosurfaces, $\lambda_2 = -10$. From (*a*) to (*d*): $t/T = 0.5, 0.75, 0, 0.25$; T is the period for $\beta = 10$. Approximately one spanwise wavelength is shown; note the compression of the ξ-axis.

Finally, the finger vortices are pulled into the swirling motion induced by the primary vortex, forming vortex tubes around it and horseshoe vortices above it. There is some indication that prior to breakdown the finger-vortex instability repeats itself on the secondary structures to form tertiary rolls.

In figure 12 the footprints of the structures visible in figure 11(a, b) are shown by means of the wall-shear component $\omega_{z,s}$. The path of the transitional spots travelling downstream resembles the transitional wedges observed in experiments. The origin of

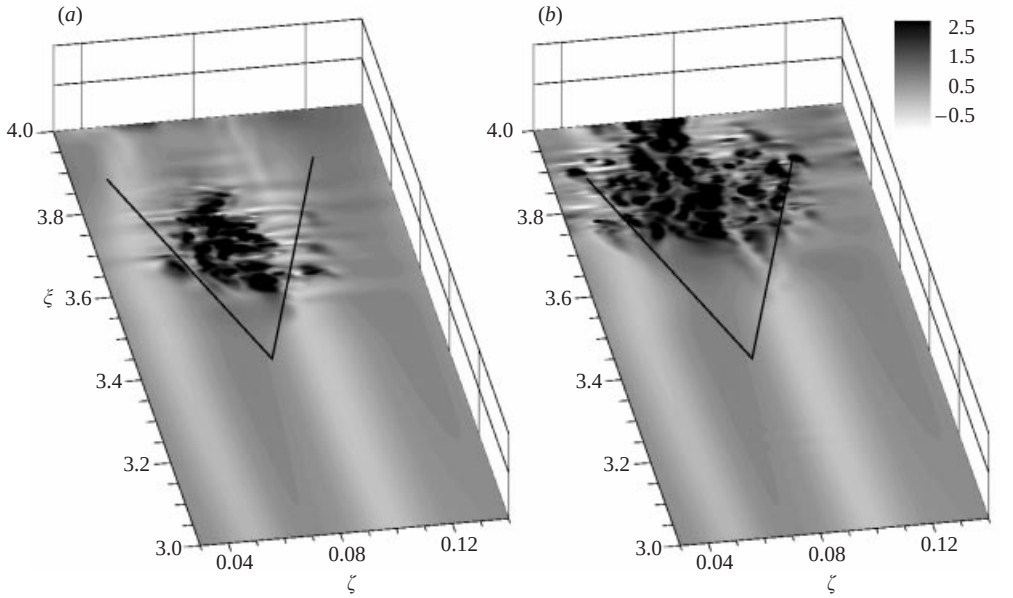

FIGURE 12. Instantaneous vorticity $\omega_{z,s}$ at the wall for Case 2B, crossflow-vortex-mode packet plus periodic background pulses: (*a*) $t/T = 0.5$, (*b*) $t/T = 0.75$; T is the period for $\beta = 10$. The resulting turbulent wedge is sketched. Approximately one spanwise wavelength is shown; note the compression of the ξ-axis.

the wedge ($\xi \approx 3.4$, $\xi \approx 0.075$) is not situated at the location where the secondary finger vortices are visible for the first time; rather it lies slightly downstream of the region where their lower ends have been drawn down to the wall, forming flat bases. The disturbances at the wall cannot be seen until the cascade of secondary vortices starts to break down. In the spanwise direction the origin of the wedge lies precisely underneath the left, near-wall tip of the dominating high-frequency secondary instability (cf. figure 9*b*).

To corroborate the convective nature of the secondary instability mechanism, the excitation of the periodic background pulses was switched off after some time. Then the unsteady field disturbances convect downstream and the flow field eventually relaxes fully to a steady state (figure 13). We note that the damping zone only starts far downstream, 60% of the distance along the region shown. Figure 14 shows the temporal evolution of the disturbance amplitudes, with an analysis time interval T. Here also the fast regrowth of the crossflow vortices can be seen (cf. figures 11, 13), indicating the persistence of these flow structures even in early turbulence. The convective nature could have already been anticipated from the possible time-accurate marching to the steady state in the pure vortex-mode-packet Case 2 with the three-dimensional disturbances suddenly introduced. We note that for parametric studies on absolute/convective instability it is appropriate to employ the linear-impulse-response method based on DNS, as used by Delbende, Chomaz & Huerre (1998) for Batchelor vortices. The method employed here is however closely related, and follows the idea of defining a finite, representative set of unsteady modes to facilitate the analysis of nonlinear mode interaction.

Another possible way of providing the necessary high-frequency background disturbances is the excitation of a primary unstable, monofrequency packet of crossflow

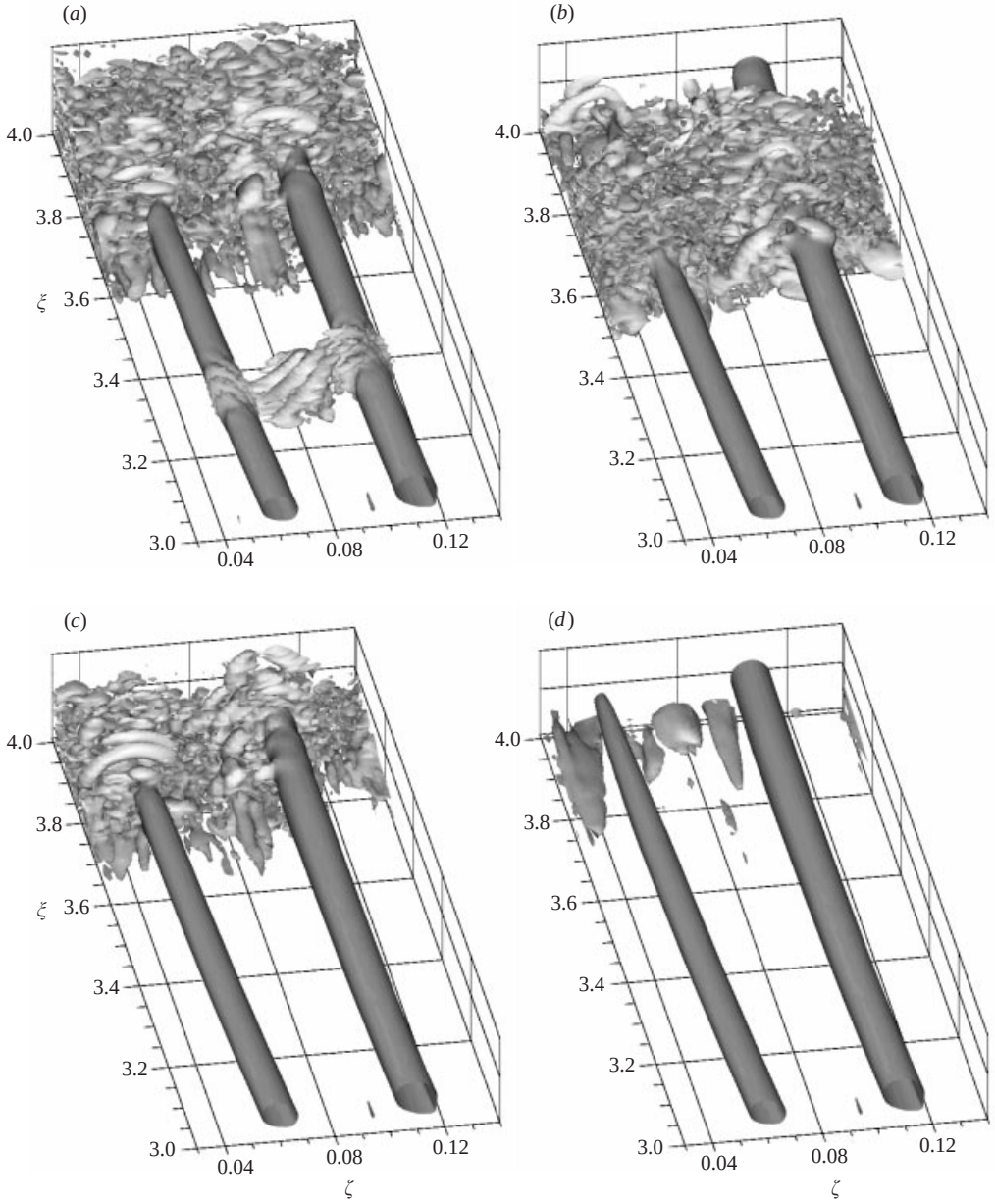

FIGURE 13. Visualization of vortical structures by λ_2-isosurfaces in the instantaneous flow fields for Case 2B, crossflow-vortex-mode packet plus periodic background pulses, after the background pulses are turned off at $t = t_0$. From (*a*) to (*d*): $t/T = t_0 + 0.85T$, $t_0 + 1.45T$, $t_0 + 2.05T$, $t_0 + 2.65T$ ($\lambda_2 = -10$, T is the period for $\beta = 10$). Approximately one spanwise wavelength is shown; note the compression of the ξ-axis.

waves, here with an amplitude that is 20% of the vortex-mode packet amplitude. In this Case 2WP a monofrequency packet of primary crossflow waves with $\beta = 20$ has been superimposed on the crossflow-vortex-mode packet, with the same spatial v'-disturbance velocity distribution within the disturbance strip at $x_2 = 0.68$, but sinusoidally varied in time. Thus the modes $(1, \pm k)$, $k = 1$–4, have been added, the

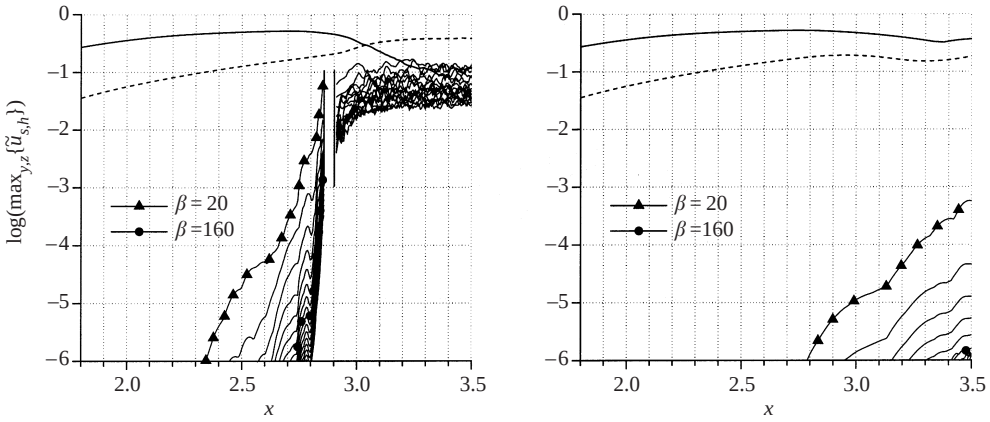

FIGURE 14. Downstream t-modal amplitude development ($\tilde{u}_{s,h}$-maximum over y and z) for Case 2B with the excitation of the periodic background pulses switched off at $t = t_0$. (a) $t = t_0 + 3T$, (b) $t = t_0 + 6T$ ($T = 2\pi/10.0$: time period with respect to $\beta = 10$).

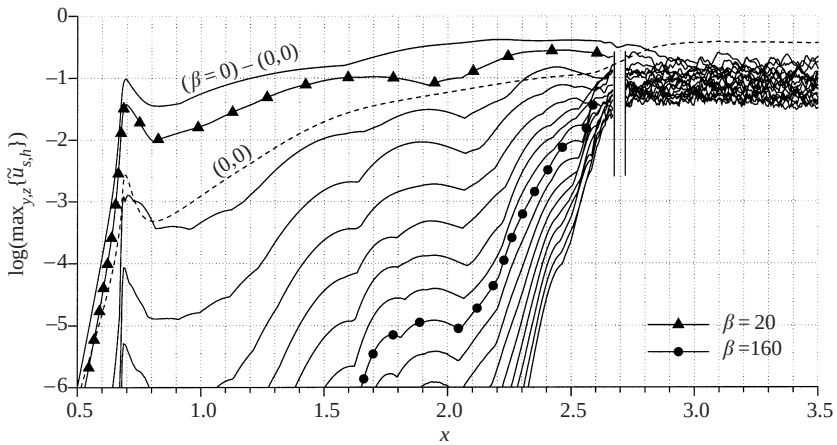

FIGURE 15. Downstream t-modal amplitude development ($\tilde{u}_{s,h}$-maximum over y and z) for Case 2WP: crossflow-vortex-mode packet plus packet of primary crossflow waves. Frequencies from $\beta = 0$ to $\beta = 320$ ($\Delta\beta = 20$) are shown. The curves to the left of the two vertical lines are obtained from second time-derivative analysis.

frequency corresponding to 1.4 times the frequency of the integrally most amplified mode. From figure 15 it can be seen that the amplitudes monotonically decrease with increasing frequency because, initially, the higher frequencies are generated non-linearly by the fundamental modes. Thus, the amplification by secondary instability starts at a different respective amplitude level compared to Case 2 and no outstandingly amplified frequency can be identified. But from the amplitude contour plot in figure 16, principally the same instability mechanism can be detected, with strong amplification of the disturbances on the left updraught side of the dominant crossflow vortex. Here, however, both a 'z' and 'y' mode can be identified. The 'y' mode seems to be involved whenever the amplified high-frequency modes are higher frequency harmonics of primarily unstable crossflow disturbances. This is consistent with DNS findings for the DLR base flow (cf. Bonfigli & Kloker 2000).

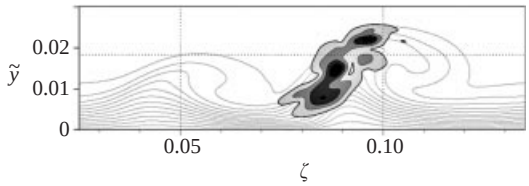

FIGURE 16. Isocontours of normalized $\tilde{u}_{s,h}$-amplitude for $\beta = 160$ for Case 2WP, crossflow-vortex-mode packet plus packet of primary crossflow waves, in a crosscut at $\xi = 3.2$. Isolines from 0.15 to 0.95 with a 0.2 spacing are shown and the deformed mean flow is indicated by the dotted lines.

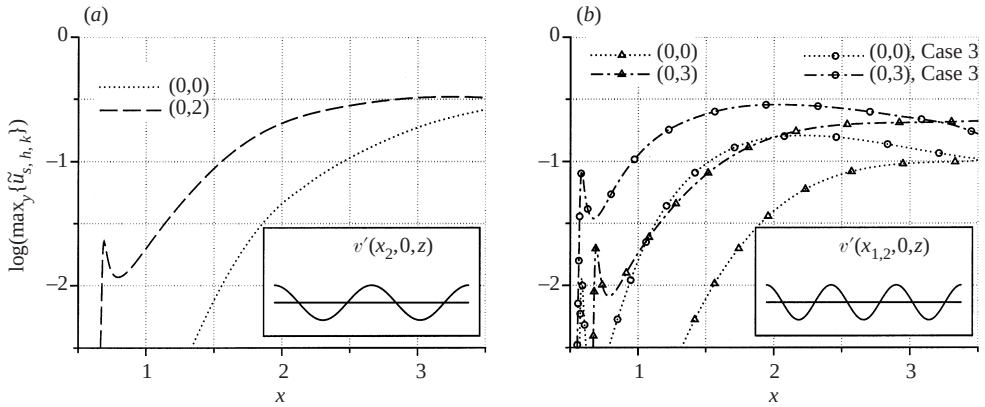

FIGURE 17. Downstream (t-z)-modal amplitude development ($\tilde{u}_{s,h,k}$-maximum over y) of single crossflow vortex modes in Case 3 (a) and Case 4 (b). Insert: normalized spanwise distribution of the forcing v'-velocity in the respective x-centre of the disturbance strip.

4.3. *Primary growth and nonlinear saturation of single crossflow-vortex modes*

In previous numerical investigations of secondary instability (see e.g. Högberg & Henningson 1998; Malik *et al.* 1999) crossflow-vortices induced initially by a single crossflow-vortex mode have been considered, although spanwise roughness rows in experiments induce packets of crossflow-vortex modes as primary disturbances. To scrutinize the effects and the importance of crossflow-vortex mode superposition on the saturation amplitude and secondary instability we have performed two reference simulations with single crossflow-vortex modes as primary disturbances. First, the integrally most amplified mode (0,2) was under investigation (Case 3) and second, the locally most amplified mode (0,3) is considered as single mode disturbance (Case 4). The crossflow vortex modes are introduced at $x_2 = 0.68$ with an amplitude of $A_{(0,k)} = 0.005Re^{1/2}$ and are strongly amplified first by primary instability. In Case 3 the mode (0,2) saturates at $x \approx 3.2$ with an amplitude level of 33% (see figure 17a, note that double-spectral amplitudes are shown), and its amplitude development coincides with the development in the crossflow-vortex-mode packet Case 2, demonstrating again the dominance of this mode in the latter case. In Case 4 the mode (0,3) does not really attain saturation in the integration domain, and therefore the excitation amplitude was increased to $A_{(0,3)} = 0.02\ Re^{1/2}$, resulting in a saturation amplitude level of 28% at $x \approx 2.0$ (figure 17b). A spanwise cut through the vortex structures in figure 18 reveals that for narrower spanwise spacing the extent of the individual vortices (plots a, e) is smaller as well as the induced localized deceleration in physical space (dashed lines in plots b, f).

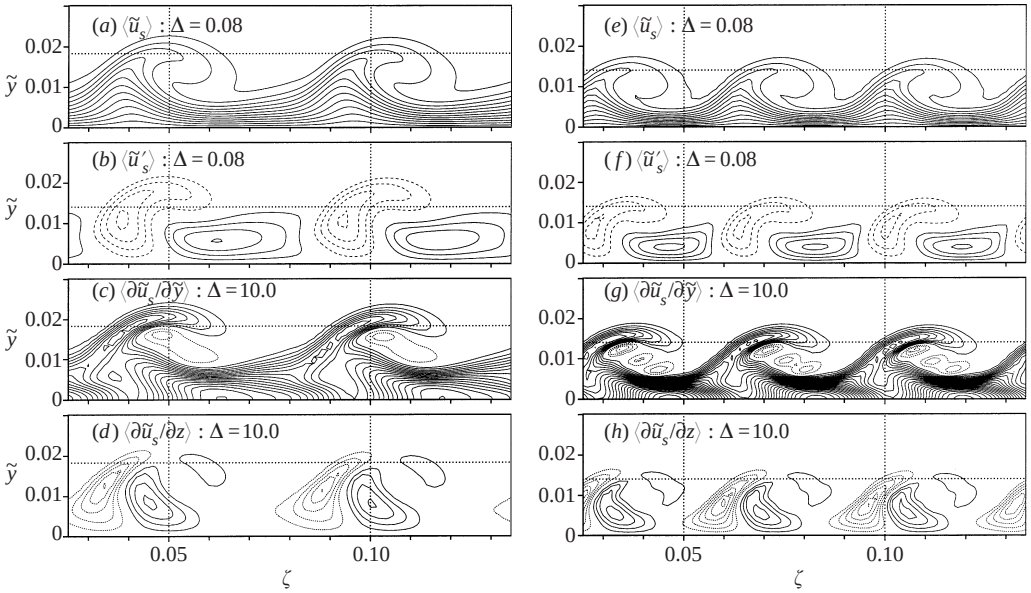

FIGURE 18. Flow field distorted by the nonlinearly saturated crossflow vortex modes in a crosscut in the vortex-oriented system: (a, e) deformed mean flow; (b, f) deformation of the mean flow; (c, d) and (g, h) y- and z-gradient of the deformed mean flow (negative isolines are dashed). Left: Case 3, single crossflow vortex mode (0,2), $A_{(0,2)} = 0.005$, at $\xi = 3.2$; Right: Case 4, single crossflow vortex mode (0,3), $A_{(0,3)} = 0.02$, at $\xi = 2.2$. To scale ($\tilde{y} = yRe^{-1/2}$).

For wavelengths larger than $\lambda_z = 2\pi/90$ the saturation level is observed to be nearly constant, whereas it decays monotonically for closer spanwise spacing, i.e. smaller λ_z. Obviously the ratio between the boundary-layer thickness and the vortex 'diameter' is the limiting quantity for large-wavelength vortices. For smaller wavelengths a large ratio between vortex diameter and the spanwise distance between the vortices strongly inhibits further growth. If the distance narrows, the co-rotating vortices have a suppressing effect on each other since the fluid motion induced by neighbouring vortices in between the vortices are of opposite direction, i.e. upward and downward, respectively.

4.4. *Secondary instability initiated by single crossflow-vortex modes*

Corresponding to the scenario considered before, the saturated vortex states have been combined with the low-amplitude periodic background pulse disturbance. In the single-vortex-mode-(0,2) Case 3B (figure 19) all the background disturbances are amplified after a short transient region. Thereby the frequency component with $\beta = 40$ attains the highest amplitude first, but further downstream it is overtaken by the most amplified frequency mode with $\beta = 140$. In comparison to the crossflow-vortex-mode packet the amplification rates, especially of the HF instability, are rather low at first, and therefore the LF instability is clear-cut in this case. The LF and HF modes exist side by side over a long distance downstream, up to $x \approx 3.3$, without any noticeable interaction. It is conspicuous that the amplification of the HF component $\beta = 140$ changes significantly at $x \approx 2.8$ from decreasing amplification to nearly constant exponential growth. Koch *et al.* found in their theoretical results a coalescence of (exponentially) growing modes and conjectured that this may translate into an observable algebraic growth. Such a coalescence seems to happen here. At $x = 2.8$

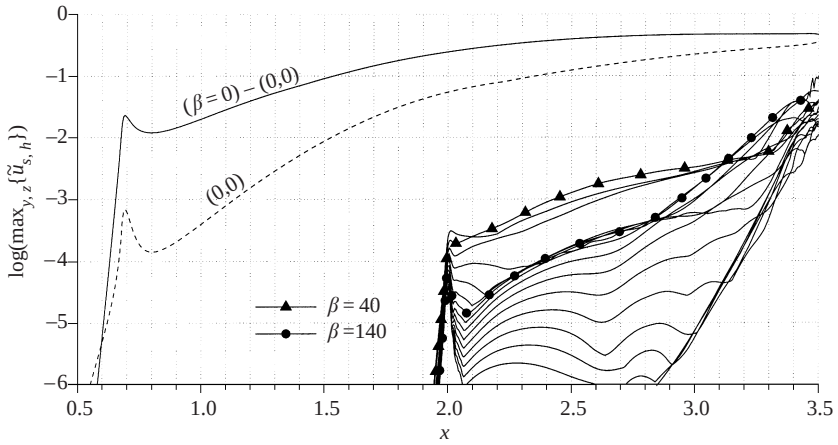

FIGURE 19. Downstream t-modal amplitude development ($\tilde{u}_{s,h}$-maximum over y and z) for Case 3B: single crossflow-vortex mode (0,2) plus periodic background pulses. Frequencies from $\beta = 0$ to $\beta = 320$ ($\Delta\beta = 20$) are shown. The curves for $\beta \geqslant 20$ are obtained from second time-derivative analysis.

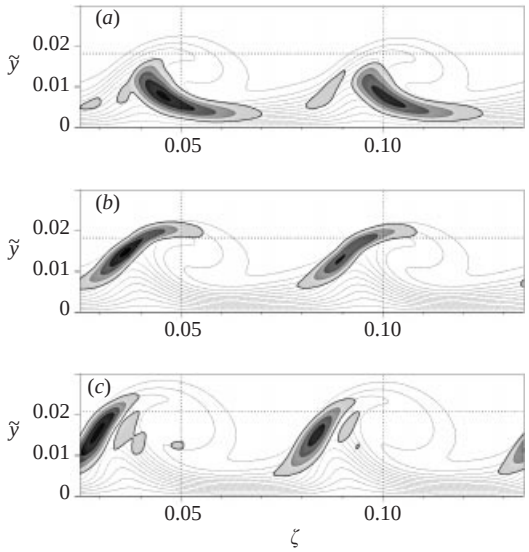

FIGURE 20. Isocontours of normalized $\tilde{u}_{s,h}$-amplitude in a crosscut in the vortex-oriented system for (a) $\beta = 40$ at $\xi = 3.2$, (b) $\beta = 140$ at $\xi = 3.2$ and (c) $\beta = 140$ at $\xi = 3.8$ for Case 3B: single crossflow-vortex mode (0,2) plus periodic background pulses. Isolines from 0.15 to 0.95 with a 0.2 spacing are shown and the deformed mean flow is indicated by the dotted lines.

one distinct secondary mode wins out over the other modes and clearly dominates further downstream. Isocontours of the $\tilde{u}_s$-amplitude for $\beta = 40$ and $\beta = 140$ in the crosscut corresponding to figure 18 show the typical shape for the LF and HF instability (see figure 20), which precisely coincide with earlier numerical results from Högberg & Henningson (1998), Koch *et al.* (2000) and experimental measurements by Kawakami *et al.* (1999), and White & Saric (2002).

In the single-vortex-mode-(0,3) Case 4B (figure 21) a totally different result arises, because first all the background disturbances are neutrally stable or even damped.

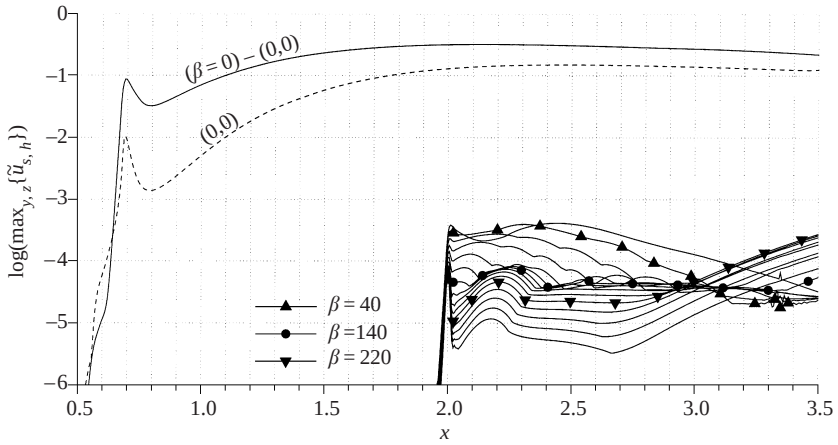

FIGURE 21. Downstream t-modal amplitude development ($\tilde{u}_{s,h}$-maximum over y and z) for Case 4B ($A_{(0,3)} = 0.02$): single crossflow-vortex mode (0,3) plus periodic background pulses. Frequencies from $\beta = 0$ to $\beta = 320$ ($\Delta\beta = 20$) are shown. The curves for $\beta \geqslant 20$ are obtained from second time-derivative analysis.

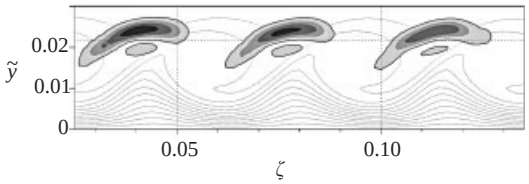

FIGURE 22. Isocontours of normalized $\tilde{u}_{s,h}$-amplitude in a crosscut in the vortex-oriented system for $\beta = 220$ at $\xi = 4.0$ for Case 4B: single crossflow-vortex mode (0,3) plus periodic background pulses. Isolines from 0.15 to 0.95 with a 0.2 spacing are shown and the deformed mean flow is indicated by the dotted lines.

A long transient region is followed by a weak amplification of some high-frequency components with β around 220. Figure 22 shows that these disturbances are connected to the wall-normal gradient. It seems that the narrow vortex spacing inhibits the 'z' mode and favours the 'y' mode, the latter being less affected by the spanwise vortex congestion. The growth however is relatively weak.

4.5. *Secondary instability: conclusions*

From the cases discussed the following conclusions can be drawn. The secondary instability is localized in physical space, i.e. fixed to the primary vortical structures, and appears in the low-momentum upwelling region, where the spanwise gradients in the mean flow especially become extreme. Two relevant types of instabilities, both clearly being of convective nature, can be observed: a strongly amplified high-frequency (HF) secondary-instability disturbance situated at the position of maximum negative spanwise gradient, and a weakly amplified low-frequency (LF) disturbance, which is connected to the maximum positive spanwise gradient. Both correspond to amplified 'z' modes found also in previous investigations using either DNS (Högberg & Henningson 1998) or secondary instability theory (Koch *et al.* 2000; Malik *et al.* 1999). At larger amplitudes of the full secondary disturbance spectrum manifold nonlinear interactions are active and a feedback effect from HF modes to LF modes can be observed. A mode connected to the wall-normal gradient, the 'y' mode, could

be observed either for the case where the HF disturbances are at first higher harmonics of primary modes, or where the primary vortices have a spanwise wavelength smaller than the most amplified steady modes. Those '*y*' modes seem of less importance for the transition process since their amplification is weak, and they could not be observed in the physically more relevant cases.

The characteristics of the secondary instability strongly depend on the development and nonlinear saturation of the primary crossflow-vortex modes with respect to the disturbance frequencies, amplification rates, starting point and the dominance of one distinct type of instability. Summarizing, it can be pointed out that a regular distribution of vortical strength, i.e. a pattern of equal vortices, is less dangerous with respect to triggering secondary instability than a spanwise-modulated distribution with the same average value and individual vortices of greater strength. Comparing the crossflow-vortex-mode-packet Case 2 with the single-vortex-mode-(0,2) Case 3 it turns out that the maximum flow deformation, especially the strongest local deceleration of the mean flow is greater in Case 2. Here, a superposition of mode (0,2) with the odd modes (0,1) and (0,3) is present, resulting in a modulated weak/strong vortex pattern instead of a regular medium/medium pattern in Case 3. Thus, a packet of crossflow-vortex modes is more dangerous than a single crossflow-vortex mode. This packet effect appears not only with randomized roughnesses but also with a regular artificial roughness row with a spanwise spacing larger than the wavelength of the most amplified mode, as observed by Saric *et al.* in their '18 mm' and '36 mm' case (the 12 mm mode is most amplified). With regular subcritical – related to the wavelength – roughness spacing a regular distribution always occurs since typically only one amplified crossflow-vortex mode is included in the disturbance spectrum.

For transition prediction in crossflow-vortex-dominated flows Malik *et al.* (1999) suggested a secondary N-factor method, i.e. a streamwise integration of secondary exponential growth up to a factor e^N, $N \approx 8.5$. This method promises to work reliably but is quite expensive since both a PSE calculation of the nonlinear primary state and a set of full-spectrum secondary stability analyses have to be performed. Thus, it is desirable to have a criterion based only on the primary saturated state. The discussion below on the conditions for the onset of secondary instability is however devoted less to the exact prediction of the transition onset than to understanding the different secondary stability properties of the primary states considered within the framework of this paper.

When searching for a condition for the onset of secondary instability, one way is to look at the maximal negative spanwise gradient, which definitely gives the location of the largest amplitude growth. Comparing the gradients for the different simulations renders this condition inappropriate however, because in the stable single-vortex-mode-(0,3) Case 4 this gradient attains nearly the same values as in the unstable cases (see figure 23*a*). Note that the smaller the spanwise spacing, the smaller the saturation amplitude, and both effects approximately compensate for the spanwise gradient. Thus, the spanwise gradient turns out to be unsuitable to compare scenarios with a different spanwise spacing of the primary vortices. More appropriate is the average value of maximum and minimum $\tilde{u}_s$-disturbance (figure 23*b*) as used, *inter alia*, by the DLR-Göttingen team. However we believe that the $\tilde{u}_s$-maximum is irrelevant and this value possibly averages out crucial differences in the more relevant maximum local deceleration of the mean flow (figure 23*c*). A minor flaw of the latter condition is that the location of the maximum deceleration and the position of the maximal negative z-gradient do not coincide. Obviously, it is difficult to correlate the secondary-instability onset with a single distinct flow quantity. It seems more physically sound to consider

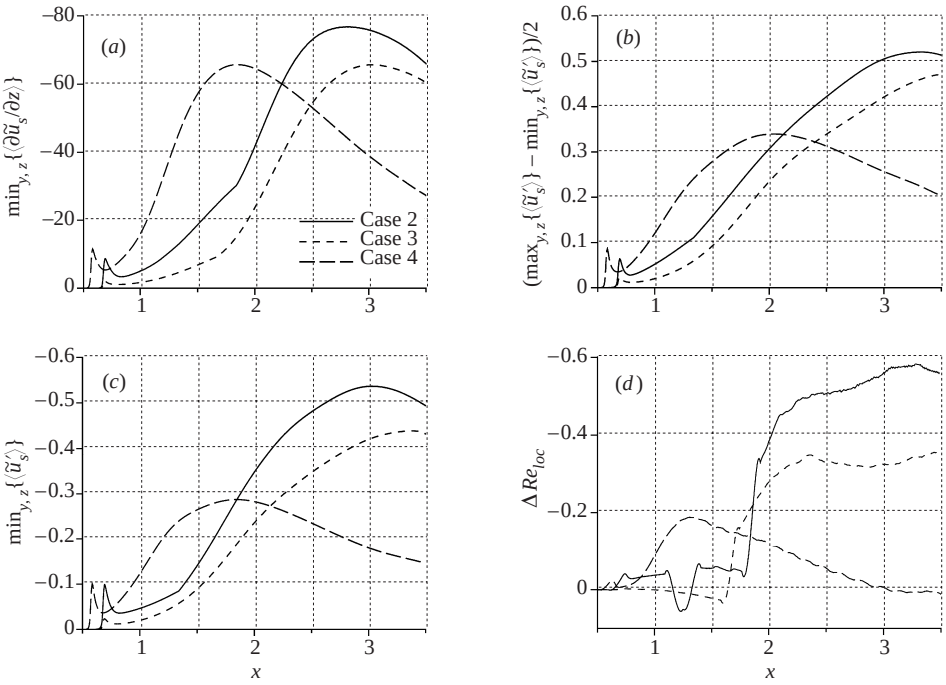

FIGURE 23. Downstream development of the three-dimensional deformation of the time-averaged mean flow $\langle\tilde{u}_s\rangle$: (*a*) minimum *z*-gradient, (*b*) average of minimum and maximum disturbance, (*c*) maximum localized mean-flow deceleration, (*d*) local Reynolds number variation. The secondary instability onset is located at $x \approx 2.1$ for Case 2 and at $x \approx 2.4$ for Case 3. In Case 4 no secondary instability occurs.

the combined action of several flow characteristics. Following considerations of Poll (1984) a *local Reynolds number variation* ΔRe_{loc} seems appropriate (figure 23*d*), using the local mean flow deceleration $\langle\tilde{u}'_s\rangle$ and the wall-distance of the location (y_0, z_0) of the maximal negative spanwise gradient (recall that an overbar denotes dimensional quantities, and $\tilde{u}_s = \bar{u}_s/\bar{u}_{s,B,e}$):

$$Re_{grad} = \frac{\langle\bar{u}'_s(\bar{y}_0, \bar{z}_0)\rangle\bar{y}_0}{\bar{\nu}}, \quad Re_{\delta_1} = \frac{\bar{u}_{s,B,e}\bar{\delta}_1}{\bar{\nu}}$$

$$\Rightarrow \Delta Re_{loc} = Re_{grad}/Re_{\delta_1} = \langle\tilde{u}'_s(y_0, z_0)\rangle\frac{y_0}{\delta_1}. \tag{4.1}$$

In our cases we find $\Delta Re_{loc} \leqslant -0.3$, here equivalent to $\langle\tilde{u}'_s\rangle_{min} \leqslant -0.3$, for the onset of secondary instability induced by a steady crossflow vortex.

5. Transition delay by 'upstream flow deformation'

For transition delay on swept wings typically suction at the wall is used. However, this method is technically complicated and costly, and has not really proven to work reliably in a satisfactory manner, at least when hole arrays are used. Compared to spanwise slits, suction holes can induce unstable three-dimensional vortex disturbances. Our DNS experiences of hole-array suction (cf. Messing & Kloker 2000) led us to believe that, at relevant suction rates, the induced crossflow-vortex packets eventually interact nonlinearly in a complex way and thus a transition delay may in some

cases be due more to non-designed crossflow-vortex interactions/suppressions rather than to the pure two-dimensional suction effect. Also, the mean flow distortion (0,0) generated nonlinearly by (uncritical) crossflow vortices may be of more importance than the 'pure' suction distortion (0,0).

Recently a different method for transition delay has been reported by Saric, Carrillo & Reibert (1998*a*), continued by White & Saric (2000), using the upstream flow deformation (UFD) technique, as we name it. The basic idea of this method is to directly influence the crossflow-vortex modes most dangerous for triggering secondary instability in a technically simple fashion, in which a spanwise row of artificial roughnesses is attached near the leading edge, with a roughness spacing smaller than the wavelength of the most amplified mode. By exciting an only weakly unstable crossflow-vortex mode with comparably small spanwise wavelength the naturally growing vortices are hindered in growth. The investigations discussed so far have shown that narrow-spaced vortices are less unstable with respect to secondary instability. The crossflow vortex modes with wavenumbers greater than that of the most amplified mode generate only primary stable higher spanwise harmonics and attenuate further downstream. This scenario holds at first only for quasi-linear or weakly nonlinear stages. However, it has been observed that a strong interaction of the crossflow vortex modes is present in nonlinear stages, i.e. the mode attaining an amplitude of about 10% first dominates the scenario by suppressing the other modes. These findings substantiate the method of Saric *et al.* to force high-amplitude crossflow vortices with 3/2 the basic wavenumber of the most amplified crossflow-vortex mode upon the flow to suppress the most destabilizing modes and thus to push downstream the onset of the secondary instability mechanisms. Malik *et al.* (1999) and Janke & Balakumar (1999) have performed some PSE-based investigations on the nonlinear interaction and suppression of steady crossflow vortex modes, but from all these investigations no conclusive explanation of the mechanisms acting can be drawn yet, and it is not clear if the results are valid only for a very specific situation.

In the simulations presented here this strategy is applied first to the pure crossflow-vortex-mode-packet Case 2 to investigate the effect on the individual packet components (§ 5.1). Secondly, the UFD is applied to Cases 2B and 2WP to quantify the modification in the secondary instability mechanism and thus the delay of transition (§ 5.2). Thereby two different excitation amplitudes for the UFD mode are considered.

5.1. *Modification of the primary state*

In Case 5 an excitation amplitude $A_{(0,3)}$ for the UFD mode (0,3) of 2% at $x_1 = 0.57$ has been chosen (figure 24*a*). The UFD mode is strongly amplified first, also generating a large two-dimensional mean flow distortion (0,0), and attains a maximum amplitude of 27% at $x = 1.91$; thereafter it decays and at $x = 3.0$ the amplitude is 14%. Compared to the packet Case 2, the growth of the other crossflow-vortex modes is clearly weakened. Only after $x = 2.8$ is the UFD mode overtaken in amplitude. A much stronger influence arises in Case 6 (figure 24*b*), when the excitation amplitude for the UFD is increased to 5%. The growth is not only weakened but there is even initial amplitude decay such that all amplitudes are at least a factor of 4 lower than in the low-amplitude-UFD Case 5 at $x = 2.5$. The mode (0,3) saturates at $x = 1.8$ with 29% and decays somewhat afterwards. Here, the UFD mode remains the largest crossflow vortex mode throughout the whole integration domain.

In our previous investigations (see Wassermann & Kloker 2000) we have also considered the modes (0,4) and (0,5) for the UFD, but with these modes the amplitude level necessary for a significant effect of the UFD cannot be realized. The

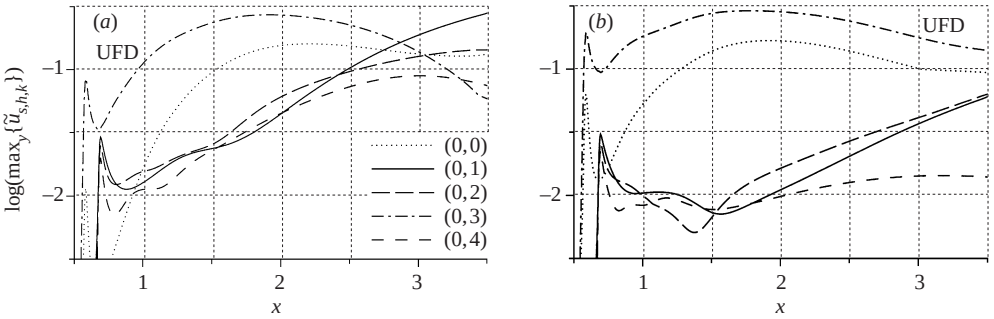

FIGURE 24. Downstream (t-z)-modal amplitude development ($\tilde{u}_{s,h,k}$-maximum over y) in (a) Case 5 ($A_{UFD} = 0.02$) and (b) Case 6 ($A_{UFD} = 0.05$).

modes (0,4) and (0,5) are strongly damped very soon downstream and on the other hand, the excitation amplitude cannot be increased arbitrarily due to a nonlinear self-suppression effect arising for very high forcing amplitudes. In these cases the generated two-dimensional mean-flow distortion becomes very large and independent, and suppresses the three-dimensional disturbances. Briefly, within the computational spanwise raster a wavelength of 2/3 of the most amplified mode turns out to be the optimum for the UFD mode.

5.2. *Transition delay*

Next, these steady scenarios were combined with the low-amplitude, periodic background pulse disturbance, excited at $x_3 = 2.0$. The downstream amplitude development is shown in figure 25(a) for the low-amplitude-UFD Case 5B and in figure 25(b) for the high-amplitude-UFD Case 6B. In Case 5B the secondary high-frequency mechanism is still active but the amplification turns out to be less than in the reference Case 2B and the most amplified frequency is shifted towards the lower value $\beta = 90$. In Case 6B any instability is virtually absent up to $x = 3.0$ and laminar breakdown is not at hand. To corroborate these results, in Case 6B the background disturbances have been also introduced at $x = 1.0$ and $x = 1.5$ (see the extra curve sets in figure 25). Here, a relatively strong local amplification can be observed, but present only for a short distance downstream, and subsequently the high-frequency components are only weakly amplified, whereas the low-frequency components are even damped. With all the excitation positions considered here all unsteady components remain below an amplitude of 1% throughout the whole integration domain.

The UFD strategy has also been applied to the vortex-mode packet plus a packet of primary crossflow waves (Case 2WP), confirming the results above. With a 2% UFD mode the transition location is shifted from $x \approx 2.6$ to $x \approx 3.25$, and no transition can be observed in the integration domain in the case with 5% UFD.

An explanation for the excellent results from the UFD in Case 6 can be found by comparing the local mean-flow decelerations of Cases 2, 5 and 6, the reference case, the low- and high-amplitude UFD Case. In figure 26 the distortion is shown in crosscuts at the ξ-position where either the secondary instability sets in or the deformation attains its maximum value, and in figure 27 the downstream development of the local maximum flow deceleration is plotted. It appears that the maximum deceleration, a co-criterion for the secondary instability, significantly decreases with the use of the UFD. This effect is much stronger than could be expected from the different saturation levels of the dominating spectral modes, because in physical space all modes, also those

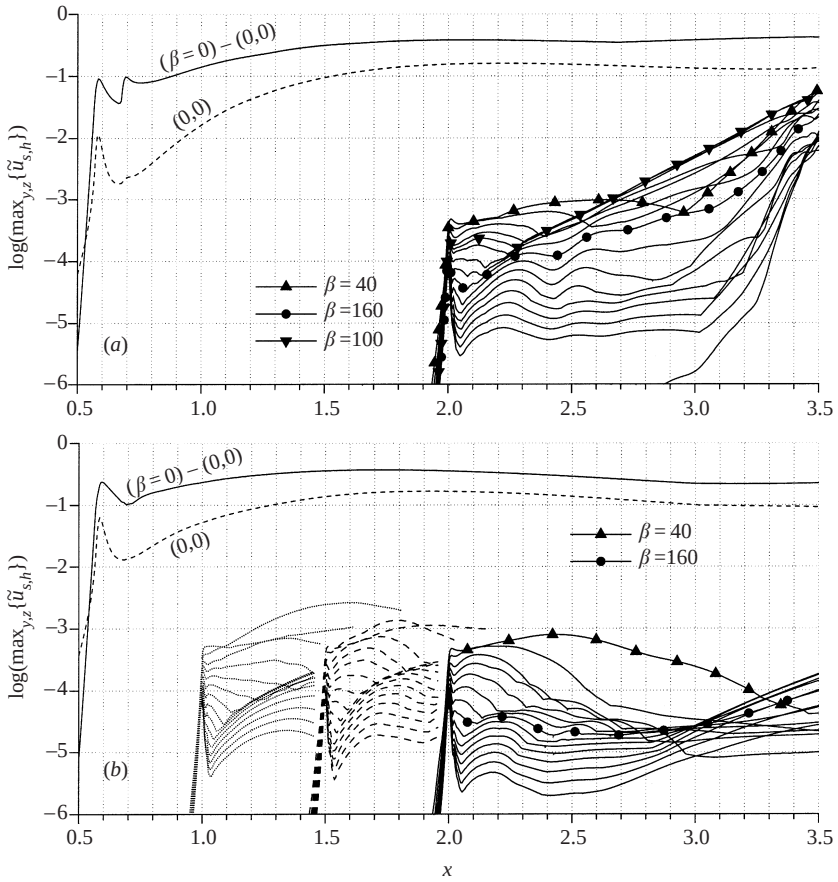

FIGURE 25. Downstream t-modal amplitude development ($\tilde{u}_{s,h}$-maximum over y and z) for Cases 5B ($A_{UFD} = 0.02$, a) and 6B ($A_{UFD} = 0.05$, b): vortex packet plus upstream flow deformation plus periodic background pulses. Frequencies from $\beta = 0$ to $\beta = 320$ ($\Delta\beta = 20$) are shown. The two extra curve sets in the bottom figure show the initial amplitude development of the background pulses if they are forced at $x = 1.0$ (dotted) and $x = 1.5$ (dashed), respectively.

nonlinearly generated, superimpose and intensify the three-dimensional distortion of the mean flow. Thus it is much more instructive to consider a t-modal rather than a t-z-modal decomposition. The deceleration in the UFD cases attains its maximum value far upstream and does not exceed a threshold value. The remaining amplification in the low-amplitude-UFD Case 5B can be explained by means of the crosscuts in figure 26(c, d). Here the crossflow-vortex packet effect, discussed before, is obvious. Due to the growing and superposition of the crossflow-vortex-packet modes, one of the streamwise vortices becomes more pronounced ($\zeta \approx 0.06$), and the maximum local mean-flow distortion (figure 27) for $x \geqslant 1.8$ is greater than in the high-amplitude-UFD Case 6B, although the amplitude of the dominating mode (0,3) is less. Moreover, especially the left-neighbouring vortex is significantly smaller and possibly allows the evolution of the 'z' mode, which is located in between the vortices and is otherwise inhibited due to the narrow vortex spacing.

For clarifying the influence of the z-phase relation between the UFD mode and the crossflow-vortex-mode packet we have performed two additional simulations. In our previous investigations (Wassermann & Kloker 1999) we found that this relation

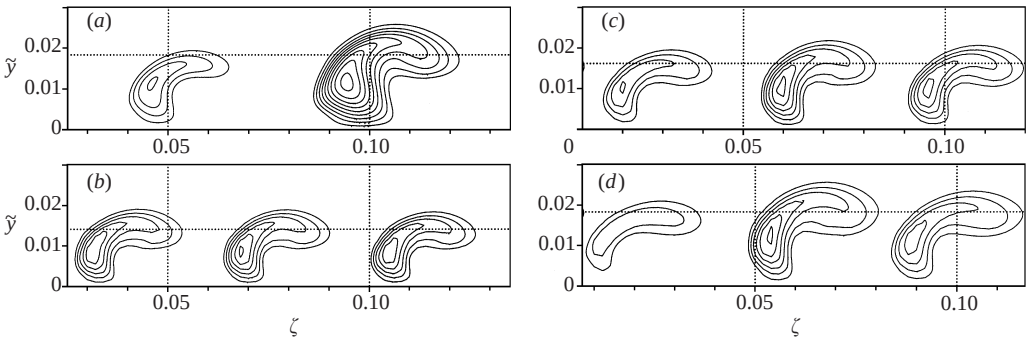

FIGURE 26. Mean-flow distortion $\langle \tilde{u}_s' \rangle$ by the nonlinearly saturated crossflow vortex modes in crosscuts in the vortex-oriented system at various ξ-positions for Cases 2, 5 and 6 (reference case, low- and high-amplitude-UFD case). (*a*) Case 2, $\xi = 3.2$; (*b*) Case 6, $\xi = 2.2$; (*c*) Case 5, $\xi = 2.7$; (*d*) Case 5, $\xi = 3.2$. Negative isolines with a 0.05 spacing are shown.

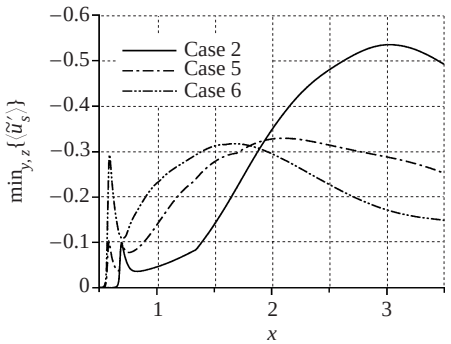

FIGURE 27. Downstream development of the maximum mean flow deceleration ($\langle \tilde{u}_s' \rangle$-minimum over y and z) with and without UFD.

has a significant influence on the suppression of the vortex-mode-packet components. To clarify this issue, Cases 5 and 6 were rerun with the z-phase of the UFD mode shifted by π. The suppression of the vortex-mode-packet components slightly changed, without any significant effect on the secondary instability properties of the deformed flow. The z-phase relation has no crucial effect as long as the UFD-mode amplitude is large enough to clearly dominate, i.e. the importance of the phase relation grows with decreasing dominance of the UFD mode.

5.3. *Role of two-dimensional mean-flow distortion*

Of great interest is the role of the two-dimensional mean-flow distortion (0,0), nonlinearly generated by the high-amplitude UFD mode. For clarification an 'adulterated' simulation (Case 7) has been performed to isolate the effect of the mode (0,0). For the adulterated simulation a modified artificial base flow has been composed by superimposing the original base flow and the mode (0,0) extracted from the high-amplitude UFD Case 6. Then we enforced the vortex-mode packet of Case 2 and simulated the modified downstream development. As can be seen from figure 28, the (0,0) part of the UFD alone is as efficient as the total three-dimensional UFD with respect to the growth attenuation. The slopes of the amplitude curves for the modes (0,1) and (0,2) nearly coincide for the Cases 6 and 7; for $x > 1.5$ the curves lie only on a higher level in the latter case. The three-dimensional part of the UFD seems just

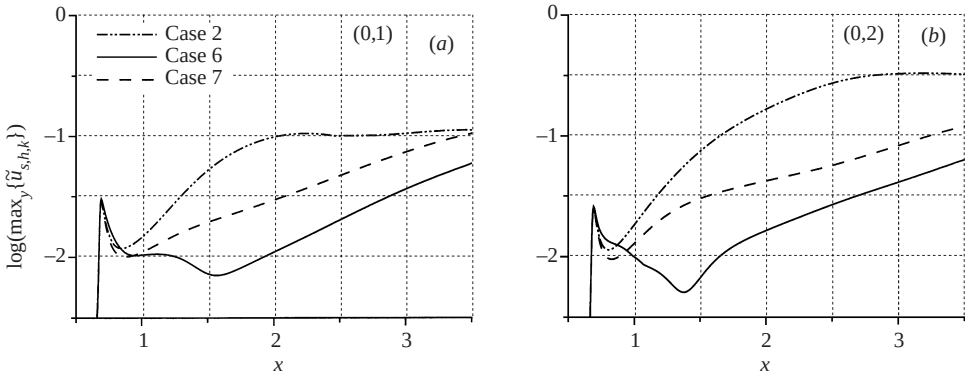

FIGURE 28. Downstream amplitude development ($\tilde{u}_{s,h,k}$-maximum over y) for the modes (0,1) (a) and (0,2) (b) in the reference Case 2, the UFD Case 6 and the adulterated Case 7.

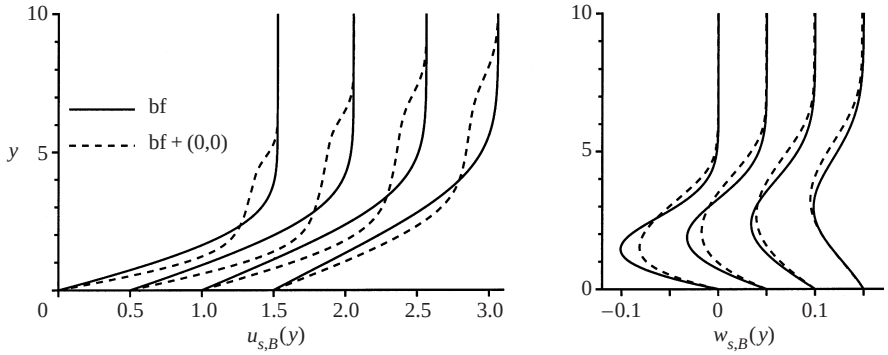

FIGURE 29. Comparison of original (bf) and distorted (bf+(0,0)) mean profiles $u_{s,B}(y)$ and $w_{s,B}(y)$ in the high-amplitude UFD Case 6 at various downstream positions ($x = 1.5, 2.0, 2.5, 3.0$ from left to right, the abscissa shift is 0.5 and 0.05, respectively).

to reduce the receptivity of the other disturbances. The modes (0,3) and (0,4) in Case 7 are suppressed even below the level in Case 6 and do not play any role at all.

A comparison of the original and the modified base flow (see figure 29) reveals the effect of the nonlinearly generated mean-flow distortion. The streamwise profiles become more bulbous in the near-wall region. For the crossflow profiles, a maximum reduction of about 20% is observed, that decreases monotonically downstream but is of relevant order throughout the region of primary crossflow instability. The mean-flow modification is quite similar to the effect of slit suction (or the (0,0) of uncritical hole-array suction).

5.4. *Effect on skin friction*

The overall goal of transition control on a swept wing is the reduction of the skin friction. The UFD strategy applied here can be evaluated theoretically from figure 30. In part (a) the local wall-normal gradient of the velocity component in the direction of the oncoming flow is plotted, which is proportional to the local skin friction coefficient c_f. It shows the increase for Case 2B due to transition, which is avoided in the UFD cases. For figure 30(b) this quantity has been integrated downstream showing the integrated effect of the UFD. At the end, the skin friction for the downstream distance considered is about 18% less.

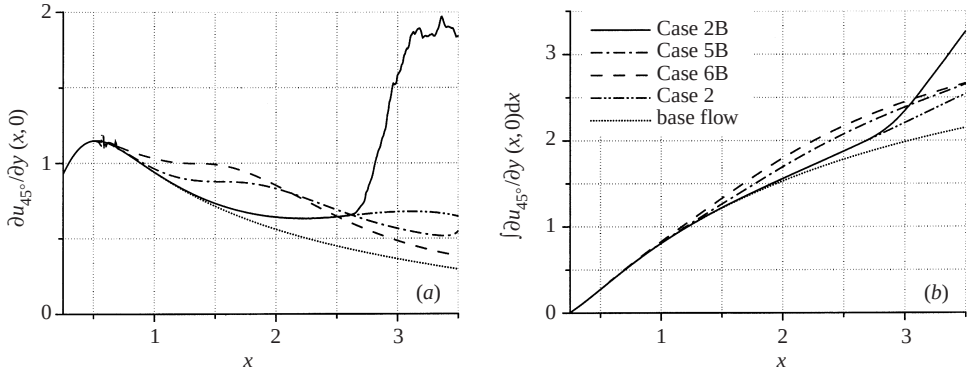

FIGURE 30. Reduction of the skin friction coefficient by the UFD. Wall-normal gradient of the time- and span-averaged velocity component in the free-stream direction $u_{45°}$, (*a*) local, (*b*) integral.

6. Conclusions

Spatial direct numerical simulations have been used to investigate nonlinear interactions, secondary instability mechanisms, and laminar breakdown for different steady crossflow-vortex scenarios in a decreasingly accelerated three-dimensional flat-plate boundary layer. We put particular emphasis on packets for primary and secondary disturbances that are more natural than single disturbance modes. The most important results are as follows.

A packet of steady crossflow-vortex modes, where the largest spanwise wavelength is larger than that of the most amplified mode, generates an irregular spanwise vortex pattern downstream with alternating strong and weak vortices. This scenario is more dangerous with respect to laminar breakdown than a scenario with equally strong vortices, often considered in investigations.

We find the onset of unsteady secondary instability clearly more connected to the maximal localized mean flow deceleration caused by the vortices than to the strength of the shear layer at the updraught vortex side.

In the upstream flow deformation (UFD) technique, the excited crossflow-vortex mode with wavelength 2/3 that of the most amplified mode leads to a regular vortex pattern downstream that nonlinearly suppresses the naturally more unstable modes. The narrow-spaced vortices saturate at lower amplitude since their further growth is hindered due to their co-rotation that leads to strong shear between two vortices. Thus the maximal local flow deformation is smaller, the vortices are less susceptible to secondary instability, and a significant transition delay results.

'Adulterated' simulations reveal that the suppression of the most amplified steady modes by UFD is to a considerable degree caused by the two-dimensional mean-flow distortion nonlinearly generated by the UFD vortices. Specifically, the two-dimensional UFD part weakens the growth, and the three-dimensional part the receptivity of the naturally growing modes.

Providing unsteady pulse disturbances for the secondary instability leads upon natural disturbance selection to a packet of small finger vortices sliding downstream at the updraught side of the large priming vortex. They are co-rotating, but in the opposite direction to the priming vortex. On travelling downstream the bottom ends are drawn down to the wall and sideways to the primary neighbouring vortex. The main parts twine around the primary vortex and are finally stretched and pulled into

the swirling main motion, forming vortex tubes around the vortex and horseshoe vortices above it. The existence of a very weak streamwise vortex, that lies close to the wall at the updraught side of the strong primary steady vortex, has no relevance for the processes observed.

On switching off the pulsing, the early (quasi-)turbulent clouds convect downstream, and the flow field settles fully to a steady state with saturated crossflow vortices. Thus, in the framework of the spatial model used with spanwise periodicity only, the existence of an absolute secondary instability can be ruled out despite the large saturation amplitudes in the clean-conditions DNS.

The financial support of this work by the Deutsche Forschungsgemeinschaft, DFG, under contract Kl 890/2 is gratefully acknowledged.

REFERENCES

Balachandar, S., Streett, C. L. & Malik, M. R. 1992 Secondary instability in rotating-disk flow. *J. Fluid Mech.* **242**, 323–347.

Bippes, H. 1997 Environmental conditions and transition prediction in 3-D boundary layers. *AIAA Paper* 97-1906.

Bippes, H. 1999 Basic experiments on transition in three-dimensional boundary layers dominated by crossflow instability. *Progr. Aerospace Sci.* **35**, 363–412.

Bonfigli, G. & Kloker, M. 1999 Spatial Navier-Stokes simulation of crossflow-induced transition in a 3-d boundary layer. In *New Results in Numerical and Experimental Fluid Dynamics II* (ed. W. G. Nitsche, H.-J. Heinemann & R. Hilbig). *Proc. 11. AG STAB/DGLR Symposium (1998)*. Notes on Numerical Fluid Mechanics, vol. 72, pp. 61–68. Vieweg.

Bonfigli, G. & Kloker, M. 2000 Three-dimensional boundary-layer transition phenomena investigated by spatial direct numerical simulations. In *Laminar-Turbulent Transition. Proc. IUTAM Symp., Sedona, AZ, USA 1999* (ed. H. Fasel & W. Saric). Springer.

Delbende, I., Chomaz, J.-M. & Huerre, P. 1998 Absolute/convective instabilities in the Batchelor vortex: a numerical study of the linear impulse response. *J. Fluid Mech.* **355**, 229–254.

Deyhle, H. & Bippes, H. 1996 Disturbance growth in an unstable three-dimensional boundary layer and its dependence on environmental conditions. *J. Fluid Mech.* **316**, 73–113.

Haynes, T. S. & Reed, H. L. 1996 Computations in nonlinear saturation of stationary crossflow vortices in a swept-wing boundary layer. *AIAA Paper* 96-0182.

Haynes, T. S. & Reed, H. L. 2000 Simulation of swept-wing vortices using nonlinear parabolized stability equations. *J. Fluid Mech.* **405**, 325–349.

Högberg, M. & Henningson, D. 1998 Secondary instability of crossflow vortices in Falkner-Skan-Cooke boundary layers. *J. Fluid Mech.* **368**, 339–357.

Janke, E. & Balakumar, P. 1999 Transition control using leading edge roughness for the ONERA-D wing. In *Mechanics of Passive and Active Flow Control. Proc. IUTAM Symp., Göttingen, Germany 1998* (ed. G. E. A. Meier & P. R. Viswanath). Kluwer.

Janke, E. & Balakumar, P. 2000 On the secondary instability of three-dimensional boundary layers. *Theoret. Comput. Fluid Dyn.* **14**, 167–194.

Jeong, J. & Hussain, F. 1995 On the identification of a vortex. *J. Fluid Mech.* **285**, 69–94.

Kawakami, M., Kohama, Y. & Okutsu, M. 1999 Stability characteristics of stationary crossflow vortices in three-dimensional boundary layers. *AIAA Paper* 99-0811.

Kloker, M. 1998 A robust high-resolution split-type compact FD scheme for spatial direct numerical simulation of boundary-layer transition. *Appl. Sci. Res.* **59**, 353–377.

Kloker, M., Konzelmann, U. & Fasel, H. 1993 Outflow boundary conditions for spatial Navier–Stokes simulations of transition boundary layers. *AIAA J.* **31**, 620–629.

Koch, W. 2002 On the spatio-temporal stability of primary and secondary crossflow vortices in a three-dimensional boundary layer. *J. Fluid Mech.* **456**, 85–111.

Koch, W., Bertolotti, F. P., Stolte, A. & Hein, S. 2000 Nonlinear equilibrium solutions in a three-dimensional boundary layer and their secondary instability. *J. Fluid Mech.* **406**, 131–174.

KOHAMA, Y., SARIC, W. & HOOS, W. 1991 A high-frequency, secondary instability of crossflow vortices, that leads to transition. In *Proc. RAS Conf. on Boundary-Layer Transition and Control, Cambridge, UK*, pp. 4.1–4.13. Royal Aeronautical Society, London.

LERCHE, T. 1996 Experimental investigations of nonlinear wave interactions and secondary instability in three-dimensional boundary-layer flow. In *Advances in Turbulence VI. Proc. Sixth European Turbulence Conf., Lausanne, Switzerland 1996* (ed. S. Gavrilakis, L. Machiels & P. A. Monkewitz). Kluwer.

LINGWOOD, R. 1997 On the impulse response for swept boundary-layer flows. *J. Fluid Mech.* **344**, 317–334.

MALIK, M. R., LI, F. & CHANG, C.-L. 1994 Crossflow disturbances in three-dimensional boundary layers: nonlinear development, wave interaction and secondary instability. *J. Fluid Mech.* **268**, 1–36.

MALIK, M. R., LI, F., CHOUDHARI, M. M. & CHANG, C.-L. 1999 Secondary instability of crossflow vortices and swept-wing boundary-layer transition. *J. Fluid Mech.* **399**, 85–115.

MAUCHER, U., RIST, U. & WAGNER, S. 1997 A method for the identification of high-frequency oscillations in unsteady flows. *Z. Angew. Math. Mech.* **77**, Suppl. 1, 209–210.

MESSING, R. & KLOKER, M. 2000 Effect of suction through arrays of holes in a 3-D boundary layer investigated by spatial direct numerical simulation. In *Laminar-Turbulent Transition. Proc. IUTAM Symp., Sedona, AZ, USA 1999* (ed. H. Fasel & W. Saric). Springer.

MÜLLER, W., BESTEK, H. & FASEL, H. 1994 Spatial direct numerical simulation of transition in a three-dimensional boundary layer. In *Laminar-Turbulent Transition. Proc. IUTAM Symp., Sendai, Japan 1994* (ed. R. Kobayashi). Springer.

POLL, D. I. A. 1984 Transition description and prediction in three-dimensional flows. *AGARD Rep.* 709 *(Special Course on Stability and Transition of Laminar Flows)*. Von Karman Inst., Rhode-St.-Genese, Belgium.

RADEZTSKY, R. H., REIBERT, M. S. & SARIC, W. S. 1999 Effect of isolated micron-sized roughness on transition in swept-wing flows. *AIAA J.* **37**, 1370–1377.

REED, H. L., HAYNES, T. S. & SARIC, W. 1998 Computational fluid dynamics validation issues in transition modeling. *AIAA J.* **36**, 742–751.

REIBERT, M. S. & SARIC, W. S. 1997 Review of swept-wing transition. *AIAA Paper* 97-1816.

REIBERT, M. S. SARIC, W. S. & CARRILLO JR., R. B. 1996 Experiments in nonlinear saturation of stationary crossflow vortices in a swept-wing boundary layer. *AIAA Paper* 96-0184.

SARIC, W. S., CARRILLO JR., R. B. & REIBERT, M. S. 1998*a* Leading-edge roughness as a transition control mechanism. *AIAA Paper* 98-0781.

SARIC, W. S., CARRILLO JR., R. B. & REIBERT, M. S. 1998*b* Nonlinear stability and transition in 3-D boundary layers. *Meccanica* **33**, 471–489.

SARIC, W. S., CARRILLO JR., R. B. & REIBERT, M. S. 1999 Control of transition in 3-D boundary layers. In *Mechanics of Passive and Active Flow Control. Proc. IUTAM Symp., Göttingen, Germany 1998* (ed. G. E. A. Meier & P. R. Viswanath). Kluwer.

SPALART, P. R., CROUCH, J. D. & NG, L. L. 1994 Numerical study of realistic perturbations in 3-D boundary layers. In *Proc. AGARD Conf.: Application of Direct and Large Eddy Simulation to Transition and Turbulence, Chania, Crete, Greece*, AGARD-CP-551, 30.1–30.10.

WASSERMANN, P. & KLOKER, M. 1999 Direct numerical simulation of the development and control of boundary-layer crossflow vortices. In *New Results in Numerical and Experimental Fluid Dynamics II* (ed. W. G. Nitsche, H.-J. Heinemann & R. Hilbig). *Proc. 11. AG STAB/DGLR Symposium (1998)*. Notes on Numerical Fluid Mechanics, vol. 72. Vieweg.

WASSERMANN, P. & KLOKER, M. 2000 DNS-investigations of the development and control of crossflow vortices in a 3-D boundary-layer flow. In *Laminar-Turbulent Transition. Proc. IUTAM Symp., Sedona, AZ, USA 1999* (ed. H. Fasel & W. Saric). Springer.

WHITE, E. B. & SARIC, W. S. 2000 Application of variable leading-edge roughness for transition control on swept wings. *AIAA Paper* 2000-0283.

WHITE, E. B. & SARIC, W. S. 2002 Secondary instability of crossflow vortices. Submitted to *J. Fluid Mech.*

WHITE, E. B., SARIC, W. S., GLADDEN, R. D. & GABET, P. M. 2001 Stages of swept-wing transition. *AIAA Paper* 2001-0271.

WINTERGERSTE, T. & KLEISER, L. 1996 Direct numerical simulation of transition in a three-dimensional boundary layer. In *Transitional Boundary Layers in Aeronautics. Proc. Colloquium*

of the Royal Netherlands Academy of Arts and Sciences, Amsterdam, NL 1995 (ed. R. A. W. M. Henkes & J. L. van Ingen). North-Holland.

WINTERGERSTE, T. & KLEISER, L. 1997 Breakdown of a crossflow vortex in a three-dimensional boundary layer. In *Direct and Large-Eddy Simulation II* (ed. J.-P. Chollet *et al.*), pp. 179–190. Kluwer.